# A HYDRAULIC FLEXIBLE JOINT ROBOT SIMULATOR

A Thesis Submitted to the

College of Graduate Studies and Research

in Partial Fulfillment of the Requirements

for the Degree of Master of Science

in the Department of Mechanical Engineering

University of Saskatchewan

Saskatoon, Canada

By

Shahram Dezfulian

# PERMISSION TO USE

In presenting this thesis in partial fulfillment of the requirements for a postgraduate degree from the University of Saskatchewan, I agree that the Libraries of this University may make it freely available for inspection. I further agree that permission for copying of this thesis in any manner, in whole or in part, for scholarly purposes may be granted by the professor or professors who supervised my thesis work or, in their absence, by the Head of the Department or the Dean of the College in which my thesis work was done. It is understood that any copying or publication or use of this thesis or parts thereof for financial gain shall not be allowed without my written permission. It is also understood that due recognition shall be given to me and to the University of Saskatchewan in any scholarly use which may be made of any material in my thesis.

Requests for permission to copy or to make other use of material in this thesis in whole or part should be addressed to:

Head, Department of Mechanical Engineering

College of Engineering

University of Saskatchewan

57 Campus Drive

Saskatoon, Saskatchewan

Canada, S7N 5A9

# ABSTRACT

The objective of this project was to design and implement an experimental hydraulic system that simulates joint flexibility of a single rigid link flexible joint robot manipulator, with the ability of changing the joint flexibility's parameters. Such a system could facilitate future control studies of robot manipulators by reducing investigation time and implementation cost of research. It could also be used to test the performance of different strategies to control the movement of flexible joint manipulators.

A hydraulic rotary servo motor was used to simulate the action of a flexible joint robot manipulator. It was a challenging task, since the control of angular acceleration was required.

A single-rigid-link, elastic-joint robot manipulator was mathematically modeled and implemented using Matlab. Joint flexibility parameters such as stiffness and damping, could be easily changed. This simulation was considered as a "function generator" to drive the hydraulic flexible joint robot. In this study the desired angular acceleration of the manipulator was used as the input to the hydraulic rotary motor and the objective was to make the hydraulic system follow the desired acceleration in the frequency range specified. The hydraulic system consisted of a servovalve and rotary motor.

A hydraulic actuator robot was built and tested. The results indicated that if the input signal had a frequency in the range of 5 to 15 *Hz* and damping ratio of 0.1, the experimental setup was able to reproduce the input signal with acceptable accuracy. Because of the inherent noise associated with the measurement of acceleration and some severe non-linearities in the rotary motor, control of the experimental test system using classical methods was not as successful as had been anticipated. This was a first stage in a series of studies and the results provide insight for the future application of more sophisticated control schemes.

# ACKNOWLEDGEMENTS

I would like to express my deepest appreciation to Professors R. T. Burton and R. Fotouhi for their advices, encouragement and patience. My special thanks go to Mr. D. V. Bitner for his technical support and never-ending help and arrangements.

I would also like to acknowledge the long-lasting support and love offered by my parents, Fraidoon Dezfulian and Afagh Delfani, my wife, Kathy Abrishami and my daughter, Shery Dezfulian.

# CONTENTS

# LIST OF TABLES

# LIST OF FIGURES

# NOMENCLATURE

$\alpha$ link angular acceleration $(rad/s^2)$

$\alpha_d$ desired angular acceleration (function generator output) $(rad/s^2)$

$\alpha_v$ link angular acceleration in volts $(v)$

$\alpha_{vc}$ link angular acceleration in volt with compensator $(v)$

$\beta$ motor viscous damping $(N \cdot m \cdot s/rad)$

$\Delta P_{12}$ nozzle pressure difference $(Pa)$

$\Delta P_{AB}$ load pressure difference $(Pa)$

$\zeta$ joint damping ratio

$\zeta_v$ valve damping ratio

$\theta$ link angular position $(rad)$

$\dot{\theta}$ link angular velocity $(rad/s)$

$\ddot{\theta}$ link angular acceleration $(rad/s^2)$

$\Theta$ Laplace transform of $\theta$ $(rad)$

$\tau$ transfer function time constant $(s)$

$\tau_1$ load time constant $(s)$

$\tau_a$ servo-amplifier time constant $(s)$

$\tau_{CL_1}$ closed-loop time constant with P controller $(s)$

$\tau_o$ open-loop time constant $(s)$

$\phi$ motor angular position $(rad)$

$\dot{\phi}$ motor angular velocity $(rad/s)$

$\ddot{\phi}$ motor angular acceleration $(rad/s^2)$

$\Phi$ Laplace transform of $\phi$ $(rad)$

$\omega$ link angular velocity $(rad/s)$

$\omega_n$ joint natural frequency $(rad/s\ or\ Hz)$

$\omega_{nv}$ valve undamped natural frequency $(rad/s\ or\ Hz)$

$a_1$ partial-fraction expansion parameter

$a_2$ partial-fraction expansion parameter

$a_3$ partial-fraction expansion parameter

$a_4$ partial-fraction expansion parameter

$a_{ac}$ measured accelerometer's acceleration $(v)$

$a_{po}$ calculated acceleration by double differentiation of position $(v)$

$A_A$ spool ring area $(m^2)$

$A_S$ spool end area $(m^2)$

$D$ joint viscous damping $(N \cdot m \cdot s/rad)$

$D_m$ motor volumetric displacement $(m^3/rad)$

$e_i$ acceleration error ($v$)

$F_1$ first term of equation 2.19

$F_2$ second term of equation 2.19

$G_{ac}$ accelerometer transfer function

$G_1$ ideal accelerometer compensator

$i_e^{'}$ servo-amplifier output current ($a$)

$I$ link moment of inertia ( $N \cdot m \cdot s^2 / rad$ )

$I_e$ input current ($ma$)

$I_e^{'}$ Laplace transform of $i_e^{'}$ ($a$)

$I_L$ link moment of inertia ($N \cdot m \cdot s^2 / rad$)

$J$ motor moment of inertia ( $N \cdot m \cdot s^2 / rad$ )

$k_1$ transfer function gain ( $rad / N \cdot m \cdot s^4$ )

$K$ joint stiffness ( $N \cdot m / rad$ )

$K_1$ load gain ( $rad / Pa \cdot s$ )

$K_a$ servo-amplifier gain ($a/v$)

$K_{CL_1}$ closed-loop gain with P controller ($s$)

$K_{con}$ conversion gain factor ($\frac{v}{rad / s^2}$)

$K_e$ servo-amplifier conversion gain ($ma/a$)

$K_I$ integral gain ($1/s$)

$K_o$ open-loop gain ( $rad / v \cdot s$ )

$K_{OL}$ open-loop overall gain ($s$)

$K_P$ proportional gain

$K_v$ valve gain ($Pa/ma$)

$l$ rotation arm ($m$)

$L$ servo-amplifier inductance ($H$)

$MSE$ mean squared error value ( $v^2$ )

$P_L$ load differential pressure ($Pa$)

$P_S$ supply pressure ($Pa$)

$R$ servo-amplifier resistance ($\Omega$)

$s$ Laplace operator ($1/s$)

$S_l$ accelerometer linear calibrated rating ($\frac{v}{m / s^2}$)

$t$ time ($s$)

$T_L$ motor torque ( $N \cdot m$ )

$u$ motor input torque ( $N \cdot m$ )

$U$ Laplace transform of $u$ ( $N \cdot m$ )

$v_e$ servo-amplifier input voltage ($v$)

$V_e$ Laplace transform of $v_e$ $(v)$

$x_{po}$ measured position $(v)$

# CHAPTER 1

# INTRODUCTION

## 1.1 Background

A robot manipulator consists of links, joints, and drive components. In order to achieve accurate robot positioning, the links and joints are usually made as rigid as possible. Rigid robot manipulators are based on the assumption that the transmissions are stiff and that the links are rigid. Such manipulators are heavy (e.g., load-carrying capacity is typically only 5% to 10% of their own weight), consume considerable power, and are generally impractical for high speed maneuvers. On the other hand, flexible manipulators have several advantages over rigid manipulators, such as smaller size and mass, rapid response, lower peak power requirements, and energy use. Light weight manipulators have links that deflect significantly in high speed operations so their flexibility cannot be ignored. Flexibility, however, can also be present in the joints.

Joint flexibility exists when there is a difference between the angular position of the driving actuator and that of the driven link. It is known that the joint flexibility can cause oscillations in robot manipulators. Therefore, when an accurate trajectory tracking of the end-effecter is needed, joint flexibility is considered as a problem [1]. In other words, joint elasticity is the main source of compliance in most current manipulator design. Joint elasticity originates from several transmitting components, such as elasticity in the gears, belts, hydraulic lines, etc. [2].

The control tasks, in case of the elastic joint manipulators, are more complicated than the equivalent rigid joint manipulators. This is true due to the fact that in the elastic joint manipulators, the number of control input torques applied by the actuators, is less than the number of degrees of freedom (DOF), also known as under-actuated systems. This happens because for each joint there is one actuator, and two degrees of freedom. This condition implies that the implementation of a "full state" feedback control task needs additional sensors for measuring the state variables of the actuator as well as the links.

The purpose of control is to appropriately deal with the oscillation created by the joint elasticity in order to get fast positioning and accurate trajectory tracking of the manipulator end-effecter. Therefore, proper control of elastic joint robot manipulators, with different characteristic expectations, and with a reasonable number of sensors, is still a challenging problem that needs to be addressed and indeed, is one of the motivating factors for this research project.

## 1.2 Literature Review

In this section several papers associated with three different topics are investigated. First dynamic modeling of flexible joint robot manipulators is brought into focus. Then different strategies for control of flexible joint robot manipulators are briefly studied. Finally a few papers regarding the analysis of hydraulic actuated robots are reviewed. It should be noted that there are other papers published on the topic of control of flexible and stiff manipulators but these are only marginally related to the topic of this thesis. The following represents a sample of the publications in this area.

Mario and Spong stated that recent experimental works showed that joint elasticity was the main source of compliance in most current manipulator designs [2]. This joint elasticity originated from several motion transmitting components, such as elasticity in the gears, belts, hydraulic lines, etc. In this paper, a single rigid link manipulator with an elastic joint was modeled. Two control solutions were derived and compared: one was

based on the feedback linearization technique, and the other one based on the nonlinear composite technique. The results indicated that the feedback linearization control needed a full state feedback (the positions and velocities of the link and motor); however, the nonlinear composite control required only the position and velocity of the link as the state feedback.

Nicosia et al examined some problems of dynamical control of manipulators with high speed continuous displacement [3]. First the rigid model was developed and then elastic and dissipative joints were included. A control strategy based on a nonlinear feedback of a model of the local joint variables was applied, and then the performance of the controlled manipulator was evaluated by means of simulation. The results showed that the use of elastic joints induced vibrations. The results were not verified experimentally.

Spong derived a simple model to represent the dynamics of elastic joint manipulators [4]. Two basic assumptions about the dynamic coupling between the motor and the link were used to derive the equations. First, it was assumed that the kinetic energy of the rotor was due to its own rotation; the second assumption was that the rotor / gear inertia was symmetric about the rotor axis of rotation. Two different control laws were then examined. The first one was the feedback linearization control, and the second one was corrective control, based on the “integral manifold law”. The results indicated that the corrective control law demonstrated better trajectory tracking.

Yu et al pointed out that their experimental investigations indicated that the joint elasticity had to be considered in the dynamics of manipulators, especially when some components, such as harmonic drives were included in the joint [5]. On the other hand, consideration of joint elasticity complicated the dynamic equations in such a manner that the current strategies for rigid joint robots control could not be used directly. In this paper, the model developed by Spong [4] was adopted. An adaptive observer control was then applied for the trajectory tracking of the robot manipulators with flexible joint. The simulation results showed that the estimated and actual link positions were well matched with the desired link position.

Albu-Schaffer and Hirzinger included the damping effects of the transmission devices in the dynamic model proposed by Spong [6]. Different control techniques were briefly discussed. It was pointed out that some techniques, such as feedback linearization, were theoretically complete, but their implementation were extremely difficult due to the measuring and / or computing of all the state variables. The proposed control strategy started using the state feedback controller; the controller gradually was extended by adding more detailed robot dynamics. The results proved that the vibrations caused by joint flexibility were effectively damped by using the proposed control technique.

Thummel et al showed that vibration induced by elastic joints could be significantly reduced by using feed forward control, based on inverse dynamic models [7]. The model consisted of the inertia of motor and link connecting by the means of a spring and a damper that described the elasticity and damping of the gearbox, respectively. Also velocity dependent, friction torques in the bearings for both motor side and link side were included. Introducing a more realistic model, the elasticity in the joint was modeled as a nonlinear spring. Some control algorithms were then reviewed. By extending the feed forward part of the controller and using the more complete robot dynamics, smaller amplitude of vibration was experienced.

Habibi et al modeled a large hydraulic robot to derive a general mathematical function for hydraulic actuation manipulators [8]. The paper focused on the dynamics of servovalve and actuator by writing the flow equations related to these components. A comparison was made among the different flow terms. It was concluded that the compression flows were significant and subsequently, they were included in the derived model.

In summary, it can be seen that some research work has been devoted to the control of the flexible joint manipulators, but more work needs to be done to fully understand the performance of the flexible joint manipulators. It is anticipated that significant advancements in this area might occur in next decades, in advancing the understanding

of the fundamentals of flexible joints and in developing practical and cost effective control laws for such manipulators.

One of the constraints that researchers have in developing control algorithms for flexible joints is verifying the approaches experimentally. At present, commercial flexible joints have either no adjustment capability or if they do, require mechanical devices which must be replaced externally. It is highly desirable to have a flexible joint in which the operating characteristics of the joint such as damping ratio and natural frequency can be adjusted "on the fly". This would allow control algorithms which have been designed to reduce the effects of flexibility in joints, to be tested under a wide range of conditions and to conditions which change in time continuously. Designing a robotic joint which would allow adjustable flexibility thus became the focus of this research.

### 1.3 Objectives

The objective of this research project was to design and implement an experimental hydraulic actuated robot manipulator that simulates robot joint flexibility in the specific range of frequencies and damping ratio with the ability of changing the joint flexibility's parameters. The damping ratio for such manipulators is normally less than 0.1 and the natural frequency between 5 to 15 *Hz* [9]. The approach that was taken in this research is as follows. A model based transfer function which represents the dynamics of flexible joint manipulators was modeled. Applying input impulse signals to the transfer function, an oscillatory angular acceleration output signal was derived by using computer based simulation. For this research project, this model based arrangement was defined as a "function generator". The output of the function generator was employed to drive an experimental hydraulic system which consisted of a servovalve and a rotary hydraulic actuator connected to a single-rigid-link manipulator. This experimental arrangement was defined as a "hydraulic simulator". The aim of the controller which drives the system was to make the hydraulic simulator reproduce the function generator signal in the specific range of frequencies and damping ratio of the function generator signal.

## 1.4 Thesis Outline

This section includes an outline of this thesis. Chapter 2 introduces the dynamic model and simulation of a flexible joint robot. Chapter 3 analyzes theoretically an actual hydraulic actuated manipulator. In Chapter 4 the experimental setup is included. Chapter 5 shows and discusses the experimental results and finally Chapter 6 concludes the results and recommends possible future works.

# CHAPTER 2

# FUNCTION GENERATOR

## 2.1 Introduction

Critical to the development of the flexible joint simulator was the "function generator" which input the appropriate signal to the hydraulic joint. The governing equations which describe the behavior of the flexible joint are considered in this Chapter. The objective of this chapter, then, is to present dynamic modeling of a single-rigid-link robot manipulator with flexible joint. The model is then simulated using typical parameters for a flexible joint in order to demonstrate the behavior of the link angular position, velocity, and acceleration for a specified torque input.

## 2.2 Governing Equations

A single-rigid-link manipulator with a revolute flexible joint is shown in Figure 2.1. In this figure, the flexible joint is modeled as a torsional spring and a torsional damper in parallel to each other (for simplicity, linear equivalent symbols of springs and dampers are adopted). $I$ and $J$ are the link and the motor moments of inertia (with respect to the center of rotation), respectively, $u$ is the motor input torque, $K$ is the joint stiffness, and $D$ is the joint viscous damping. The angles $\theta$ and $\phi$ are the angular positions of the link

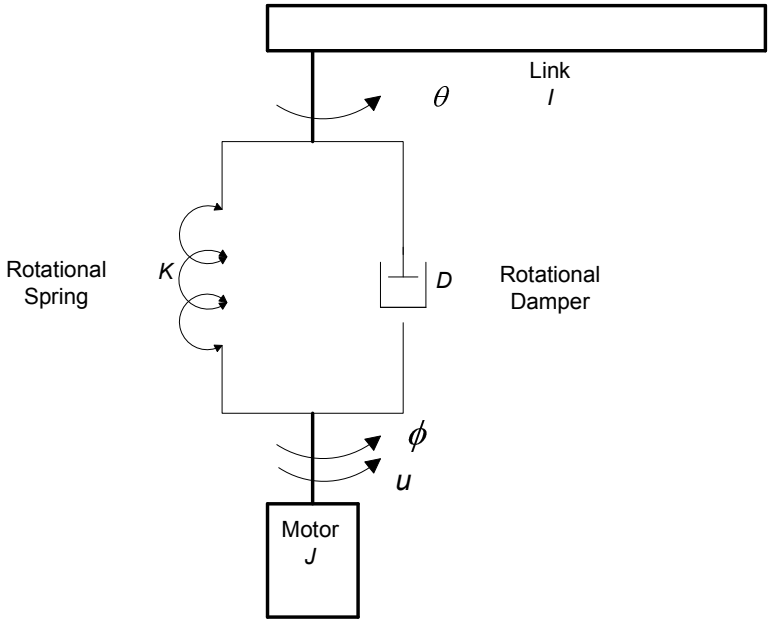


(a) Linear equivalent schematic of the single-link manipulator

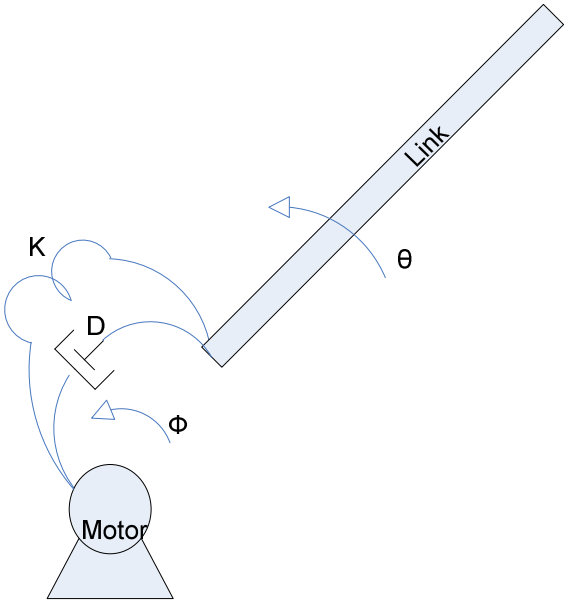


(b) Dynamic equivalent schematic of the single-link manipulator

**Figure 2.1**- Schematic of a single-link manipulator with flexible joint

and the motor, respectively. The link and motor angular positions are chosen as the generalized coordinates. The link motion is assumed to be in the horizontal plane.

Joint stiffness and damping are included in the dynamics of the model presented here. For simplicity, gravity effects are not considered in the model; this is consistent with the experimental setup (hydraulic simulator) used in this study which is a horizontal planar robot manipulator.

For the link shown in Figure 2.1 the dynamic equations are as follow:

$$I\ddot{\theta} + D(\dot{\theta} - \dot{\phi}) + K(\theta - \phi) = 0 \ , \tag{2.1}$$

$$J\ddot{\phi} + D(\dot{\phi} - \dot{\theta}) + K(\phi - \theta) = u \ , \tag{2.2}$$

or:

$$\begin{bmatrix} I & 0 \\ 0 & J \end{bmatrix} \begin{Bmatrix} \ddot{\theta} \\ \ddot{\phi} \end{Bmatrix} + \begin{bmatrix} D & -D \\ -D & D \end{bmatrix} \begin{Bmatrix} \dot{\theta} \\ \dot{\phi} \end{Bmatrix} + \begin{bmatrix} K & -K \\ -K & K \end{bmatrix} \begin{Bmatrix} \theta \\ \phi \end{Bmatrix} = \begin{Bmatrix} 0 \\ u \end{Bmatrix} \quad . \tag{2.3}$$

The input to the single link manipulator is torque $u$ which is assumed to be an impulse signal. Taking the Laplace transform of equations (2.1) and (2.2), and assuming zero initial conditions, yields:

$$Is^2\Theta(s) + D[s\Theta(s) - s\Phi(s)] + K[\Theta(s) - \Phi(s)] = 0 \quad , \tag{2.4}$$

$$Js^2\Phi(s) + D[s\Phi(s) - s\Theta(s)] + K[\Phi(s) - \Theta(s)] = U(s) \, . \tag{2.5}$$

Rearranging equations (2.4) and (2.5) gives:

$$(Is^2 + Ds + K)\Theta(s) - (Ds + K)\Phi(s) = 0 \quad , \tag{2.6}$$

$$(Js^2 + Ds + K)\Phi(s) - (Ds + K)\Theta(s) = U(s) \, . \tag{2.7}$$

Solving for $\Phi(s)$ in equation (2.6):

$$\Phi(s) = \frac{(Is^2 + Ds + K)}{Ds + K}\Theta(s) \ . \tag{2.8}$$

Substituting equation (2.8) into equation (2.7), yields:

$$\frac{(Js^2 + Ds + K)(Is^2 + Ds + K)}{Ds + K}\Theta(s) - (Ds + K)\Theta(s) = U(s) \, , \tag{2.9}$$

$$[(Is^2 + Ds + K)(Js^2 + Ds + K) - (Ds + K)^2]\Theta(s) = (Ds + K)U(s) \, , \tag{2.10}$$

$$[IJs^4 + (I + J)Ds^3 + (I + J)Ks^2]\Theta(s) = (Ds + K)U(s) \ . \tag{2.11}$$

Finally, the transfer function which relates link's rotation $\theta$ to input torque *u* is as follows:

$$\frac{\Theta(s)}{U(s)} = \frac{Ds + K}{s^2[IJs^2 + (I + J)Ds + (I + J)K]} \quad , \tag{2.12}$$

or:

$$\frac{\Theta(s)}{U(s)} = \frac{\frac{D}{IJ}s + \frac{K}{IJ}}{s^2 + (\frac{D}{I} + \frac{D}{J})s + (\frac{K}{I} + \frac{K}{J})} * \frac{1}{s^2} \quad . \tag{2.13}$$

This indicates that the undamped natural frequencies of the system are zero and $\sqrt{(\frac{K}{I} + \frac{K}{J})}$. Zero natural frequency represents the rigid body motion of the base and the link.

The block diagram of the open-loop system based on equation (2.13) is shown in Figure 2.2. In this figure:

$$k_1 = \frac{K}{IJ}, \tau = \frac{D}{K}, \quad \omega_n = \sqrt{(\frac{K}{I} + \frac{K}{J})} \text{ and } \zeta = \frac{D}{2}\sqrt{\frac{1}{K}(\frac{1}{I} + \frac{1}{J})}$$

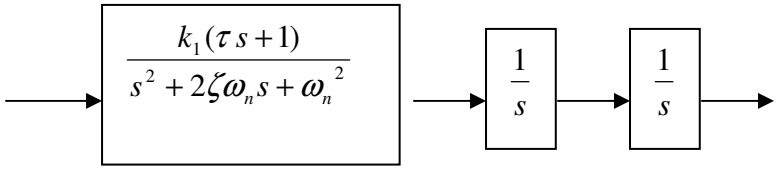


**Figure 2.2**- The open-loop block diagram of single link manipulator with flexible joint

It is evident that the system has two integrators which will significantly filter out any higher frequency perturbations which might be introduced by the joint.

The equations were implemented using MATLAB ®. In this simulation, the manipulator's physical parameters have been taken from [9] and are listed in Table 2.1:

**Table 2.1-** Simulation parameters adopted from [9]

| Symbol | Description | Quantity | Unit |
|---|---|---|---|
| $I$ | Link moment of inertia | 5.000 | $N \cdot m \cdot s^2 / rad$ |
| $J$ | Motor moment of inertia | 5.000 | $N \cdot m \cdot s^2 / rad$ |
| $K$ | Joint stiffness | 1.000E4 | $N \cdot m / rad$ |
| $D$ | Joint viscous damping | 31.63 | $N \cdot m \cdot s / rad$ |

Applying these parameters to equation 2.13 yields:

$$\frac{\Theta(s)}{U(s)} = \frac{400(0.00316s+1)}{s^2+12.65s+4000} * \frac{1}{s^2} \quad . \tag{2.14}$$

Comparing with the standard transfer function

$$\frac{\Theta(s)}{U(s)} = \frac{k_1(\tau s+1)}{s^2+2\zeta\omega_n s+\omega_n^2} * \frac{1}{s^2} \quad , \tag{2.15}$$

the natural frequency and damping ratio are as follows:

$\omega_n = \sqrt{4000} = 63.25\ rad/s\ = 10.00\ Hz$ and $\zeta = 0.10$

It should be emphasized that the range of values used in this project are quite common for flexible joint robot manipulators.

The input to the simulation was an approximate impulse (representing a torque impulse). Some of the simulation results are shown in Figure 2.3. In this particular simulation two time delayed pulse input torques with zero and 1.5$s$ phase delay, period

of 3$s$, pulse width of 0.1% of period, and amplitude of $u$ = +3000 $N \cdot m$ and $u$ = -3000 $N \cdot m$ have been used. The output results shown in the figure are the link angular position, velocity, and acceleration, respectively. It should be noted that a continuous-time integration solver of Runge-Kutta method with zero initial condition and a fixed-step size of 0.001 in seconds has been applied.

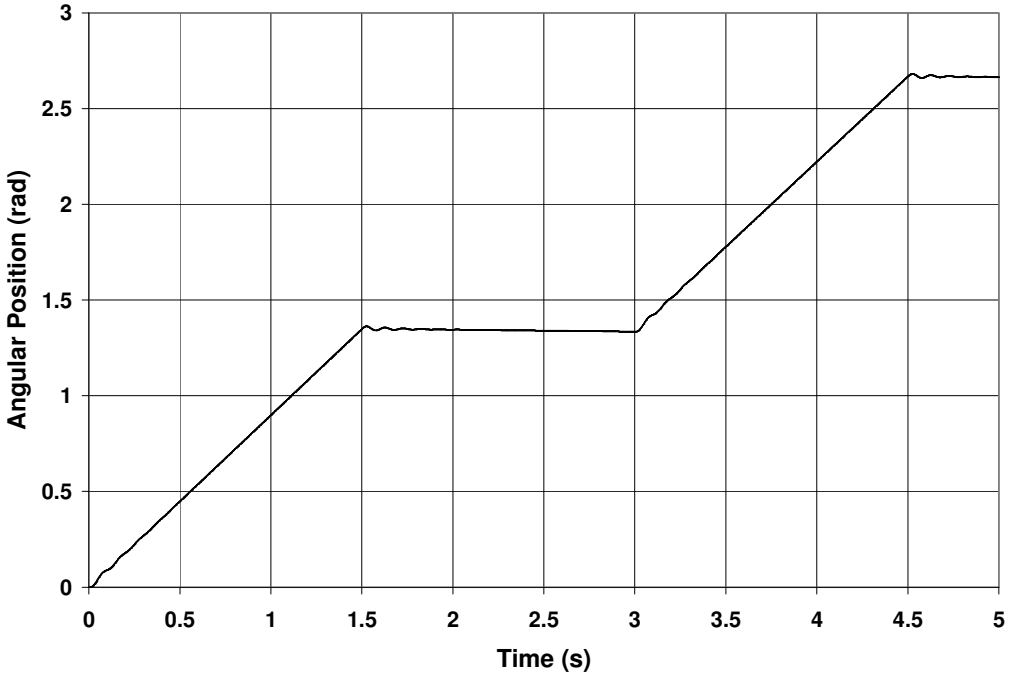


(a) Angular position

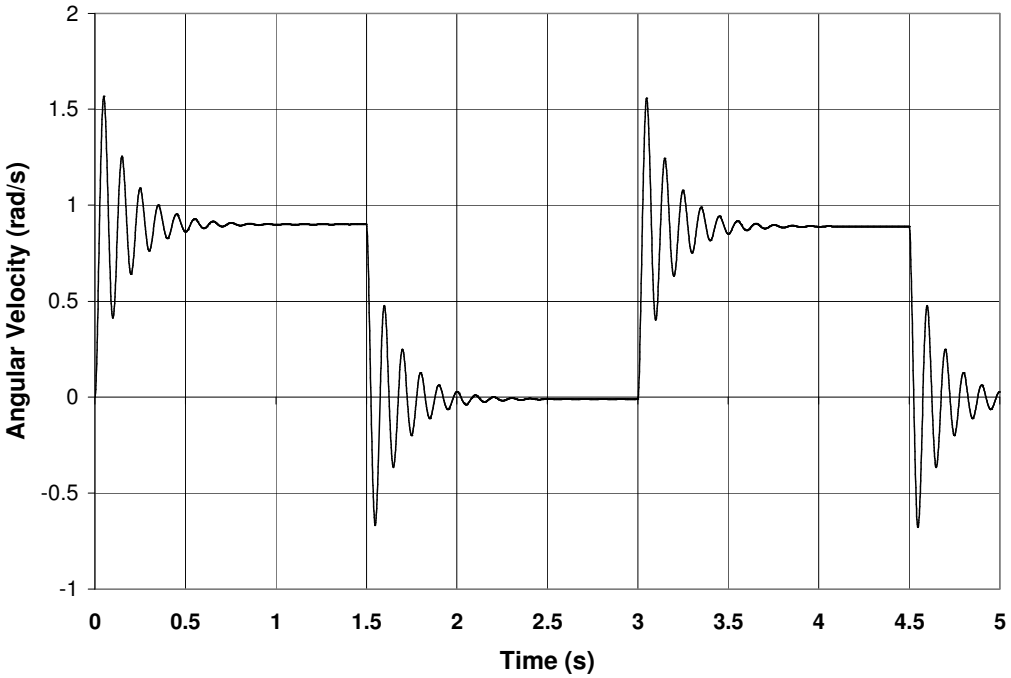


(b).Angular velocity

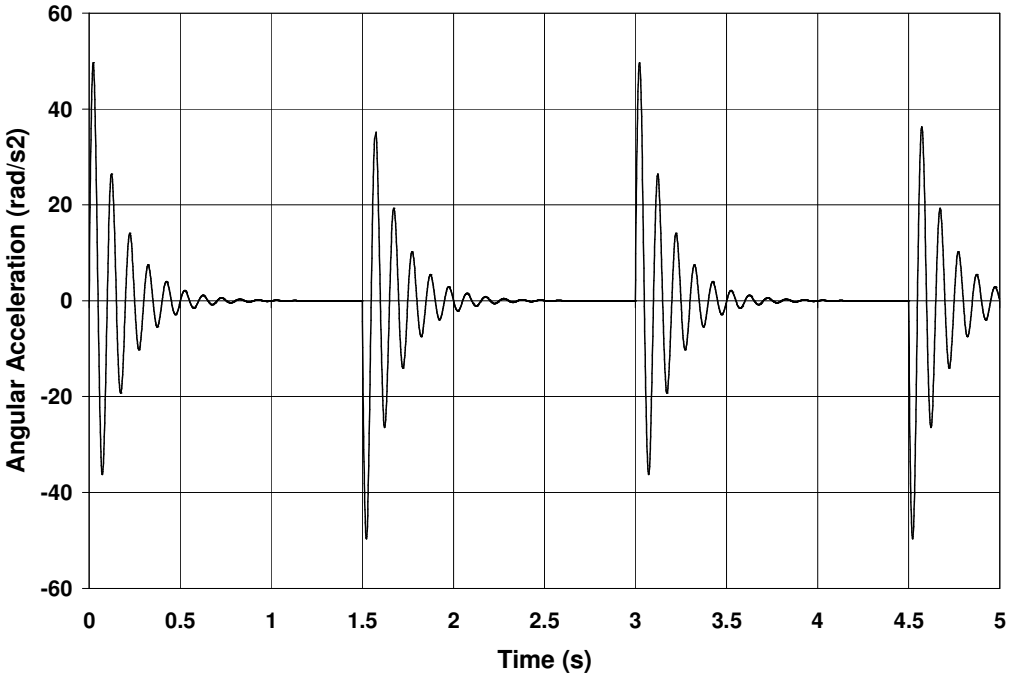


(c) Angular acceleration

**Figure 2.3**- Simulation results for impulse inputs to the single-link manipulator

The results show that by applying an impulse torque input, a damped oscillation is observable in angular acceleration and velocity, but the magnitude is highly filtered in angular position of the link. These vibrations may be felt, but not observed visually. Since torque on the joint is directly related to angular acceleration, the low damping can have significant implications when control is implemented.

A closed form solution of equations 2.14 or 2.15 does exist and can be solved by applying Partial-Fraction Expansion. Consider equation 2.14:

$$\frac{s^2\Theta(s)}{U(s)} = \frac{400(0.00316s+1)}{s^2+12.65s+4000} \quad , \tag{2.16}$$

or

$$s^2\Theta(s) = \frac{1.265s+400}{s^2+12.65s+4000}U(s)\,. \tag{2.17}$$

In order to create the same form of the input signal as the simulation (an approximate impulse), two separate step inputs are used: the first a step of 3000*N.m* at zero step time and a second step at 0.003s (0.1% of the 3s period time) step time and final value of -3000 *N.m*. In this case, $U(s) = \frac{3000}{s} - \frac{3000\,e^{-0.003\,s}}{s}$ and equation 2.17 becomes:

$$s^2\Theta(s) = \left(\frac{1.265s+400}{s^2+12.65s+4000}\right)\left(\frac{3000}{s} - \frac{3000e^{-0.003s}}{s}\right), \tag{2.18}$$

or:

$$s^2\Theta(s) = \left(\frac{3795s+1200000}{s(s^2+12.65s+4000)}\right) - \left(\frac{e^{-0.003s}(3795s+1200000)}{s(s^2+12.65s+4000)}\right) = F_1(s) - F_2(s)\,. \tag{2.19}$$

Knowing that;

$$s^2+12.65s+4000 = (s+6.325+j62.9285)(s+6.325-j62.9285)\ , \tag{2.20}$$

and the Partial-Fraction Expansion of first term of equation 2.19:

$$\frac{3795s+1200000}{s(s^2+12.65s+4000)}=\frac{a_1}{s}+\frac{a_2s+a_3}{s^2+12.65s+4000} \quad , \tag{2.21}$$

multiplying both sides by the denominator of its left hand side of equation 2.20 yields:

$$3795s+1200000=a_1(s^2+12.65s+4000)+a_2s^2+a_3s\,, \tag{2.22}$$

or

$$3795s+1200000=(a_1+a_2)s^2+(12.65a_1+a_3)s+4000a_1\,. \tag{2.23}$$

Comparing both sides of equation 2.23, it can be shown that:

$$a_1+a_2=0\,, \tag{2.24}$$

$$12.65a_1+a_3=3795\,, \tag{2.25}$$

$$4000a_1=1200000\,, \tag{2.26}$$

.

Solving, the parameters are found to be:

$a_1=300$, $a_2=-300$ and $a_3=0$.

Therefore:

$$F_1(s)=\frac{3795s+1200000}{s(s^2+12.65s+4000)}=\frac{300}{s}-\frac{300s}{s^2+12.65s+4000}\,, \tag{2.27}$$

or:

$$F_1(s) = \frac{3795s + 1200000}{s(s^2 + 12.65s + 4000)} = 300(\frac{1}{s}) - 300\frac{(s + 6.325) - 0.1(62.9285)}{(s + 6.325)^2 + 62.9285^2}. \quad (2.28)$$

Considering $F_2(s) = e^{-.003s} F_1(s)$, using equation 2.28 and applying the inverse Laplace transform to equation 2.19 yields:

$$\ddot{\theta}(t) = 300 - 300e^{-6.325t}(Cos62.9285t - 0.1Sin62.9285t)\, u(t)$$
$$-\left(300 - 300e^{-6.325(t-0.003)}[Cos62.9285(t - 0.003) - 0.1Sin62.9285(t - 0.003)]\right)u(t - 0.003) \quad (2.29)$$

Figure 2.4 shows the plot of the analytical solution of equation 2.29.

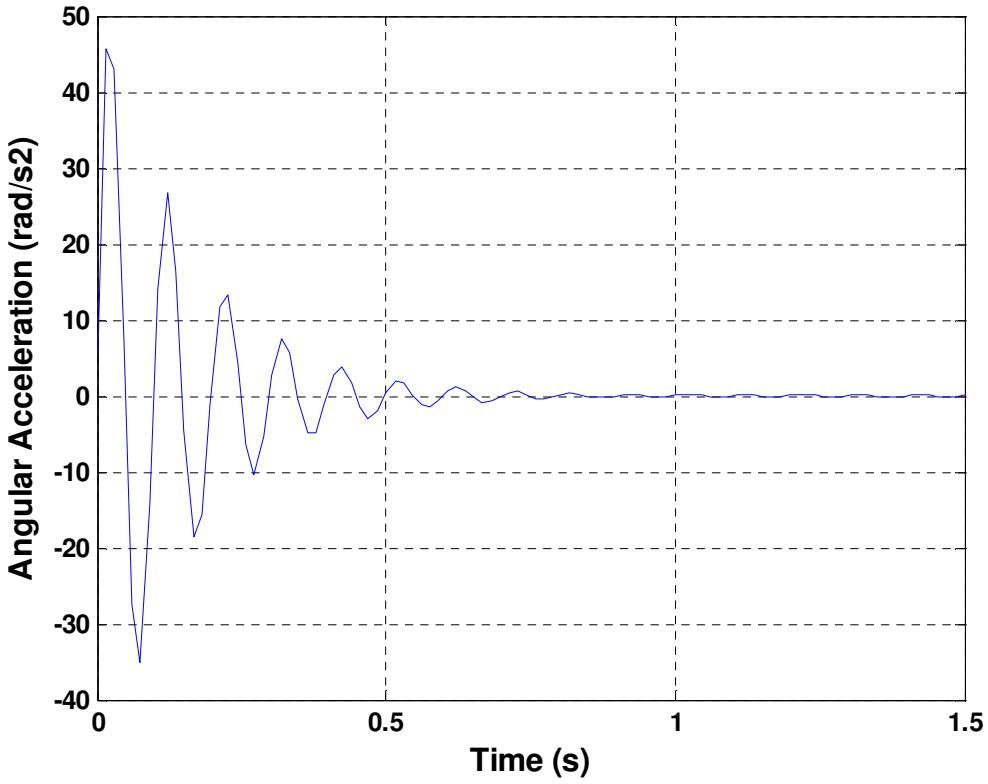


**Figure 2.4**- Plot of equation 2.29.

The two solutions for acceleration response using the computer solver and the closed solution form yield the same the results as would be expected. The function generator can be realized either from the simulation using Matlab or by implementing the closed solution form of equation 2.29. In this work, the simulation form was used because of the ease of changing the parameter values.

# CHAPTER 3

# HYDRAULIC SIMULATOR

## 3.1 Introduction

The hydraulic simulator is essentially the experimental hydraulic system which receives the input signal from the function generator and outputs an acceleration which is controlled to follow the desired input signal. The main reason for choosing a hydraulic actuation system was because of the higher value of its natural frequency in comparison to the usual robot manipulators' natural frequency. Hydraulic systems are also readily found in many robotic applications which make compatibility issues marginalized. It was recognized that the design of a system to reproduce accurately such waveforms would be a challenging process, given that acceleration tends to be noisy and difficult to control. As will be illustrated later, the presence of a severe nonlinearity (suspected to be dead-band) in the rotary motor compounded the control problem. Figure 3.1 shows the overall arrangement of the system.

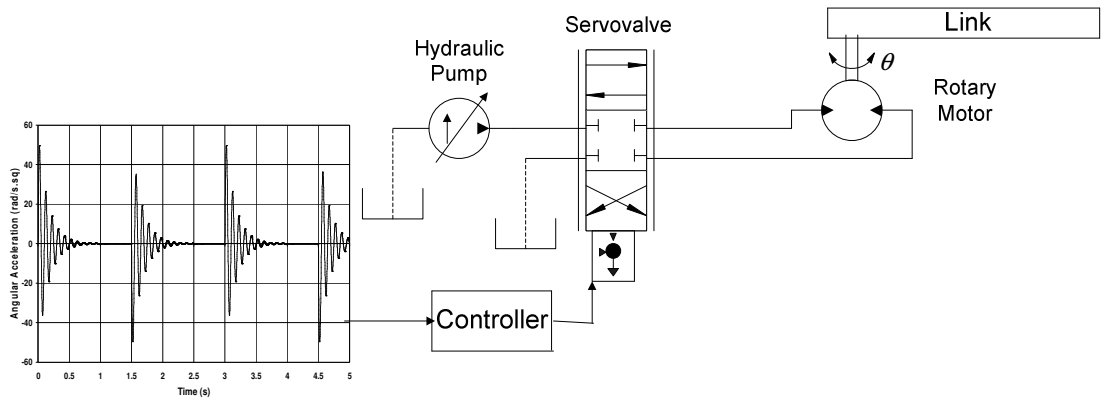


**Figure 3.1**- Schematic of the hydraulic simulator

The system shown in Figure 3.1 consisted of a pressure compensated hydraulic pump driven by an electric motor, a pressure control servovalve (MOOG® model 15-010), and a rotary motor (MICRO-PRECISION® ROTAC model MPJ-22-1V), which drove a single-link manipulator. The rotary motor could rotate the link 270º in the horizontal plane.

The measuring instruments consisted of an acceleration sensor (Bruel & Kjaer® model 4370) and amplifier (Bruel & Kjaer® charge amplifier type 2635). The experimental system was controlled by a PC computer using Matlab-Simulink® software.
A flow control servovalve was initially considered but because the flow rates were very small, because the cut-off frequency of pressure servovalves is known to be very high (relative to a flow control servovalve), and because pressure (force) is directly related to acceleration, a pressure control servovalve was chosen as the hydraulic controlling device. All components were “off the shelf” from the Fluid Power Laboratory at the University of Saskatchewan and hence, this became a constraint for the hydraulic system design.

### 3.2 Hydraulic System Analysis

As stated above, the function of the hydraulic simulator was to be able to reproduce the input signal which in this particular case was the angular acceleration signal created by the function generator. To facilitate the design of a controller, an analysis of the hydraulic system was performed.

A common form of a transfer function approximation of the relationship between the load differential pressure and the input current to the servovalve has been derived to be [10]:

$$\frac{P_L(s)}{I_e(s)} = \frac{K_v}{\left(\frac{s}{\omega_{nv}}\right)^2 + \left(\frac{2\zeta_v}{\omega_{nv}}\right)s + 1} \ , \tag{3.1}$$

in which:

$P_L$ load differential pressure ($Pa$)

$I_e$ input current ($ma$)

$K_v$ valve gain ($Pa/ma$)

$\omega_{nv}$ valve undamped natural frequency ($Hz$)

$\zeta_v$ valve damping ratio

$s$ Laplace operator ($1/s$).

The torque on the hydraulic rotary motor is given by;

$$T_L = P_L D_m = I_L \alpha + \beta \omega \ , \tag{3.2}$$

in which:

$T_L$ motor torque $(N \cdot m)$

$D_m$ motor volumetric displacement $(m^3 / rad)$

$I_L$ link moment of inertia $(N \cdot m \cdot s^2 / rad)$

$\beta$ motor viscous damping $(N \cdot m \cdot s / rad)$

$\omega$ link angular velocity $(rad/s)$

$\alpha$ link angular acceleration $(rad / s^2)$,

Taking the Laplace transform of equation 3.2 yields;

$$\frac{\omega(s)}{P_L(s)} = \frac{\frac{D_m}{\beta}}{(\frac{I_L}{\beta}s + 1)} \ , \tag{3.3}$$

or:

$$\frac{\alpha(s)}{P_L(s)} = \frac{\frac{D_m}{\beta}s}{(\frac{I_L}{\beta}s + 1)} \ . \tag{3.4}$$

let;

$K_1 = \frac{D_m}{\beta}$ and $\tau_1 = \frac{I_L}{\beta}$

therefore;

$$\frac{\alpha(s)}{P_L(s)} = \frac{K_1 s}{\tau_1 s + 1}, \tag{3.5}$$

in which;

$K_1$ load gain $(rad / Pa \cdot s)$

$\tau_1$ load time constant (*s*).

Multiplying equations 3.1 and 3.5, gives;

$$\frac{\alpha(s)}{I_e(s)} = \frac{K_v}{\left(\frac{s}{\omega_{nv}}\right)^2 + \left(\frac{2\zeta_v}{\omega_{nv}}\right)s + 1} \cdot \frac{K_1 s}{\tau_1 s + 1} \quad . \tag{3.6}$$

The following equation is valid for the servo-amplifier which should provide DC current into the servovalve:

$$v_e = i_e^{'} R + \frac{di_e^{'}}{dt} L, \tag{3.7}$$

in which:

$v_e$ servo-amplifier input voltage (*v*)

$i_e^{'}$ servo-amplifier output current (*a*)

*R* servo-amplifier resistance (Ω)

*L* servo-amplifier inductance (*H*).

Taking the Laplace transform of the equation 3.7 yields;

$$\frac{I_e^{'}(s)}{V_e(s)} = \frac{\frac{1}{R}}{\frac{L}{R}s + 1}, \tag{3.8}$$

Let $K_a = \frac{1}{R}$ and $\tau_a = \frac{L}{R}$, therefore;

$$\frac{I_e^{'}(s)}{V_e(s)} = \frac{K_a}{\tau_a s + 1}, \tag{3.9}$$

in which;

$K_a$ servo-amplifier gain (*a/v*)

$\tau_a$ servo-amplifier time constant (*s*)

It should be noted that according to [11] for the servo-amplifier, *R*=2000 Ω, *L*=9.7 *H*. Therefore $K_a = 0.0005\ a/v$ and $\tau_a = 0.00485\ s$.

Since the unit of servo-amplifier output current ($I_e'(s)$) is ampere and that of servovalve input current ($I_e(s)$) is milliampere, a conversion gain of $K_e$ is introduced to convert the units. Therefore, $K_e = 1000\ ma/a$. Applying the gain to equation 3.9 gives;

$$\frac{I_e(s)}{V_e(s)} = \frac{K_a K_e}{\tau_a s + 1}, \tag{3.10}$$

in which;

$K_e$ servo-amplifier conversion gain (*ma/a*).

Multiplying equations 3.6 and 3.10 yields;

$$\frac{\alpha(s)}{V_e(s)} = \frac{K_a K_e}{\tau_a s + 1} \frac{K_v}{\left(\frac{s}{\omega_{nv}}\right)^2 + \left(\frac{2\zeta_v}{\omega_{nv}}\right)s + 1} \frac{K_1 s}{\tau_1 s + 1} \tag{3.11}$$

The block diagram of equation 3.11 is shown in Figure 3.2.

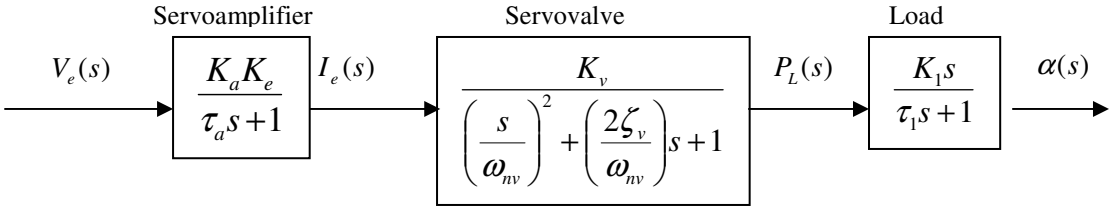


**Figure 3.2-** Block diagram of equation 3.11.

It should be noted that $\alpha(s)$ has units of rad/s$^2$.

Since $\tau_1 \rangle\rangle \tau_a$, the servo-amplifier transfer function can be reduced to $K_a K_e$. This reduced form is illustrated in Figure 3.3:

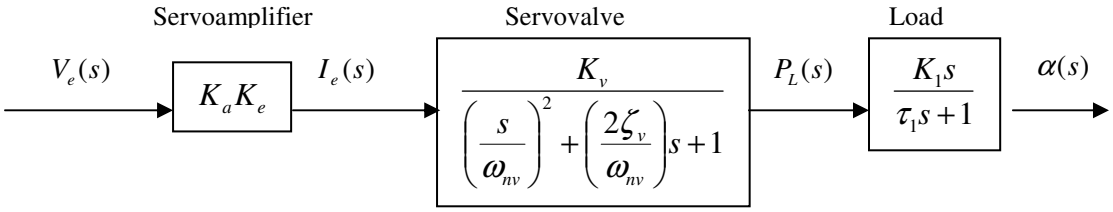


**Figure 3.3-** Reduced block diagram of equation 3.11

Now two possible scenarios are expected with respect to the transfer functions of the servovalve and the load. The first scenario occurs when $\left|\frac{1}{\tau_1}\right| \langle \left|\omega_{nv}\right|$, where $\omega_{nv}$ is now in *Hz* to ensure unit consistency. A typical magnitude asymptotic approximation (magnitude Bode plot) for this first case is shown in Figure 3.4.

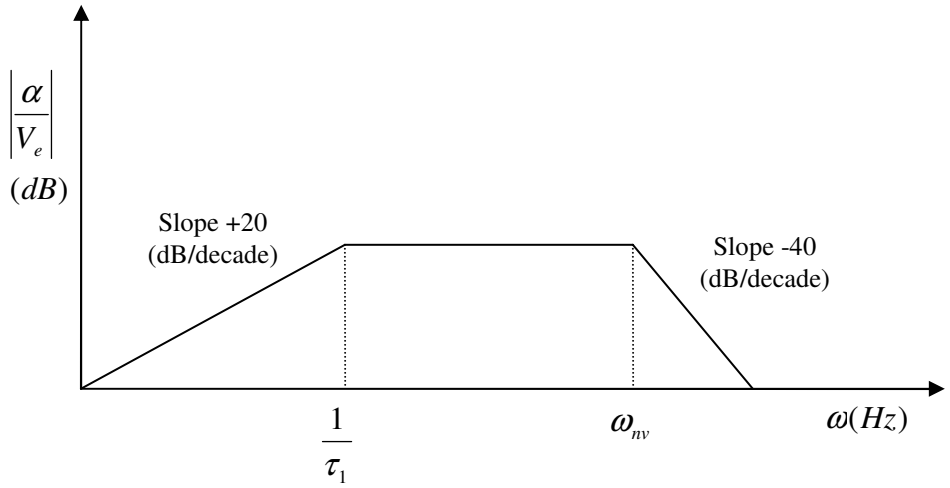


**Figure 3.4**- Typical magnitude Bode plot of equation 3.11 when $\left|\frac{1}{\tau_1}\right| \langle \left|\omega_{nv}\right|$

The second scenario happens when $\left|\frac{1}{\tau_1}\right| \rangle \left|\omega_{nv}\right|$; a typical Bode plot for this case is demonstrated in Figure 3.5.

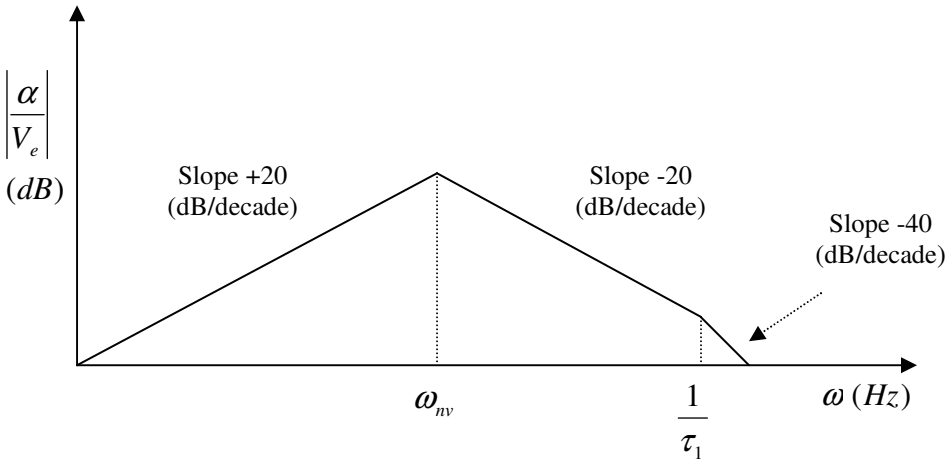


**Figure 3.5**- Typical magnitude Bode plot of equation 3.11 when $\left|\frac{1}{\tau_1}\right| \rangle \left|\omega_{nv}\right|$

The actual frequency response of the hydraulic simulator is shown in Figure 3.6, where the input is the signal from the analyzer unit and the output is the measured signal from the accelerometer. Details on obtaining this plot are given in Chapter 5.

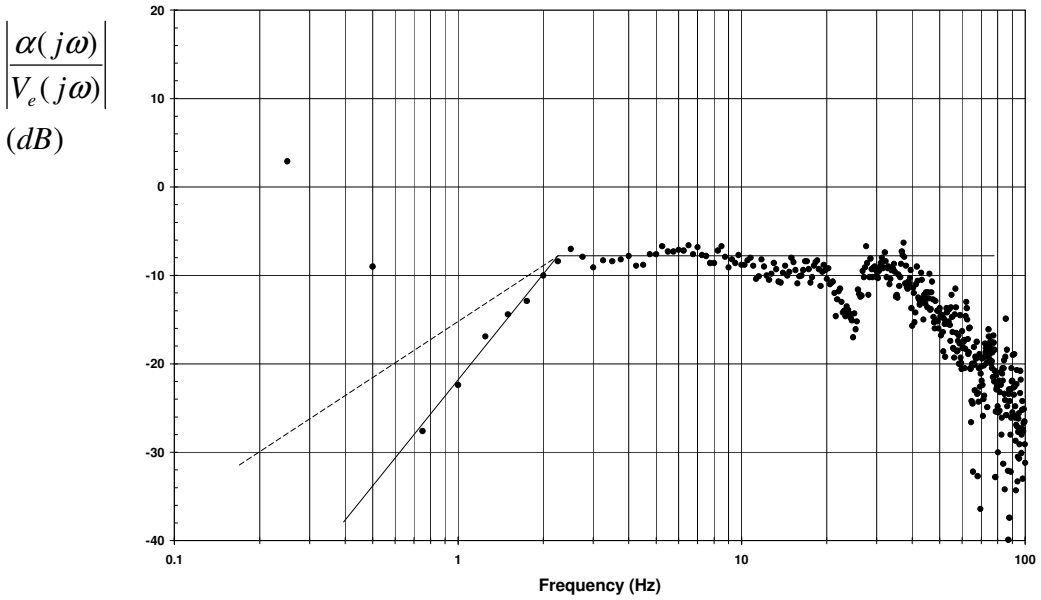


**Figure 3.6**- Open-loop magnitude frequency response of the hydraulic simulator (points) with superimposed asymptotic lines (experimental: solid line based on 40 dB per decade and theoretical: dashed line based on 20dB per decade)

It should be noted that the two odd points at lower frequencies were ignored in Figure 3.6.

A comparison between the experimental result and the theoretical scenarios shows that the first possible scenario ($\left|\frac{1}{\tau_1}\right| \langle \left|\omega_{nv}\right|$) better describes the actual experimental setup for frequencies less than 20 *Hz*.

It should be noted that the slope of asymptotic line (solid line) in Figure 3.6 is +40 dB per decade which is different from that of the theoretical model (dashed line) of Figure 3.6. Measurement of the output angular acceleration was accomplished using an accelerometer (to be discussed in greater detail below and in Chapter 4). It was believed

that the poor performance of the accelerometer at low frequencies caused the discrepancy. In the next two chapters it will be shown that an acceleration compensator could be used to correct the performance of the accelerometer at low frequencies.

These results imply that, $|\omega_{nv}| \rangle\rangle \left|\frac{1}{\tau_1}\right|$, and therefore the model could be easily reduced to the first order term of the transfer function of equation 3.11 Hence,

$$\left(\frac{\alpha(s)}{V_e(s)}\right)_{OL} = \frac{K_o s}{\tau_o s + 1} \quad , \qquad (OL \text{ in this case means open-loop.}) \tag{3.12}$$

in which;

$K_o$ open-loop gain ($rad / v \cdot s$)

$\tau_o$ open-loop time constant ($s$).

It should be noted that $K_o = K_a K_e K_v K_1$ and $\tau_o = \tau_1$. Therefore the open-loop block diagram is simplified to that shown in Figure 3.7.

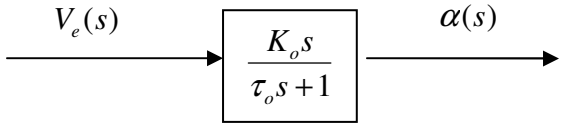


**Figure 3.7**- Simplified open-loop block diagram of the system

In the aforementioned equations, $\alpha$ has a unit of rad/s$^2$. Since a linear accelerometer was used to indirectly measure the angular acceleration of the joint, a linear sensitivity and calibration factor which converts rad/s$^2$ to voltage was introduced. The calibrated output rating of the linear accelerometer was determined to be $S_l = 0.1(\frac{v}{m/s^2})$. The linear accelerometer was capable of measuring tangential acceleration. However, it was the angular acceleration that was desired. Since the distance between the center of the installed linear accelerometer and the axis of the rotation (rotation arm) was known very accurately ($l$ = 0.435 $m$), it was possible to convert the linear tangential acceleration to

angular acceleration. By multiplying the linear sensitivity $S_l$ by $l$, the angular sensitivity (the conversion gain) of the accelerometer was obtained as:

$$K_{con} = S_l.l = 0.1(\frac{v}{m/s^2}).\,0.435\,(m) = 0.0435\,(\frac{v}{rad/s^2}) \tag{3.13}$$

The effect of the $K_{con}$ is shown in the block diagram of Figure 3.8;

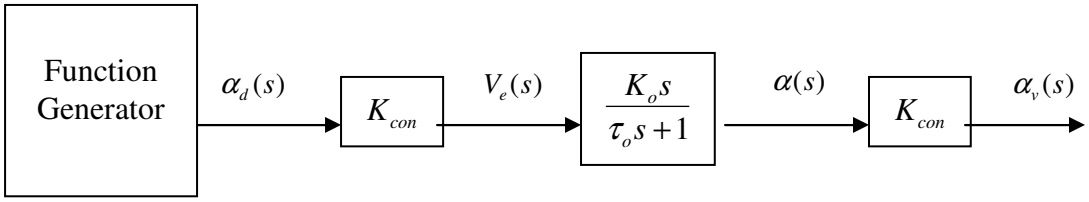


**Figure 3.8-** Block diagram of the simplified transfer function with influence of the accelerometer sensitivity

In the block diagram of Figure 3.8;

$K_{con}$ conversion gain factor $(\frac{v}{rad/s^2})$

$\alpha_d$ desired angular acceleration (function generator output) $(rad/s^2)$

$\alpha$ link angular acceleration $(rad/s^2)$

$\alpha_v$ link angular acceleration in volts $(v)$,

therefore;

$$\left(\frac{\alpha_v(s)}{V_e(s)}\right)_{OL} = \frac{K_{OL}s}{\tau_o s+1}, \tag{3.14}$$

in which;

$K_{OL}$ open-loop overall gain $(s)$.

It should be noted that $K_{OL} = K_o K_{con}$ .

### 3.3 Controller Design (Theoretical)

To design the controller which would provide the required closed-loop response, the first step was to consider the hydraulic simulator in a mathematical form and to design the controller for this system. The second step was to apply this controller to the experimental hydraulic simulator and to "tune" the controller to optimize the performance (see Chapter 5).

In this section, a closed-loop control system based on a theoretical model is studied. The closed-loop transfer function is derived and its parameters are compared with the open-loop transfer function. An approach of cascade inverse compensation for improving the open-loop system rather than using a closed-loop controller is introduced.

#### 3.3.1 Closed-Loop Controller

The objective of any controller is to force the output to follow the input such that $\left(\frac{\alpha_v(s)}{V_e(s)}\right)_{CL} = 1$ (*CL* in this case means closed-loop). This means the hydraulic simulator would follow exactly the desired signal from the function generator. This section considers the implementation of several classical controllers in an attempt to meet the above objective. For all analysis, the simplified open-loop transfer function of Equation 3.14 is assumed.

A simple proportional controller was first examined. The closed-loop block diagram is illustrated in Figure 3.9.

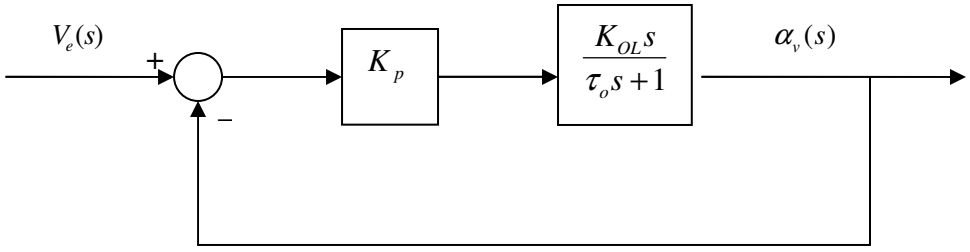


**Figure 3.9**- Block diagram of closed-loop control system with proportional gain

In Figure 3.9;

$K_P$ proportional gain

The closed-loop transfer function is derived with respect to the block diagram shown in Figure 3.9 as follows;

$$\left(\frac{\alpha_v(s)}{V_e(s)}\right)_{CL_1} = \frac{\dfrac{K_p K_{OL} s}{\tau_o s+1}}{1+\dfrac{K_p K_{OL} s}{\tau_o s+1}}, \tag{3.15}$$

which simplifies to:

$$\left(\frac{\alpha_v(s)}{V_e(s)}\right)_{CL_1} = \frac{K_{CL_1} s}{\tau_{CL_1} s+1}\ , \tag{3.16}$$

in which; $K_{CL_1} = K_p K_{OL}$ , and $\tau_{CL_1} = \tau_o + K_p K_{OL}$ .

It is clear that the objective of having $\left(\frac{\alpha_v(s)}{V_e(s)}\right)_{CL_1} = 1$ is not satisfied at all frequencies with this controller. Table 3.1 provides a comparison of the open-loop and closed-loop transfer function parameters.

**Table 3.1**- Parameters summary of open-loop and closed-loop transfer functions

| | Open-loop | Closed-loop |
|---|---|---|
| Gain | $K_{OL} = K_o K_{con}$ | $K_{CL_1} = K_P K_{OL}$ |
| Time constant | $\tau_o$ | $\tau_{CL_1} = \tau_o + K_P K_{OL}$ |

Theoretically this Table illustrates that the closed-loop control gain (if $K_P \rangle 1$) and time constant are increased in comparison to the open-loop system. Using typical parameter values, a comparison of the open-loop and closed-loop frequency responses (magnitude) for two controller gains is shown in Figure 3.10.

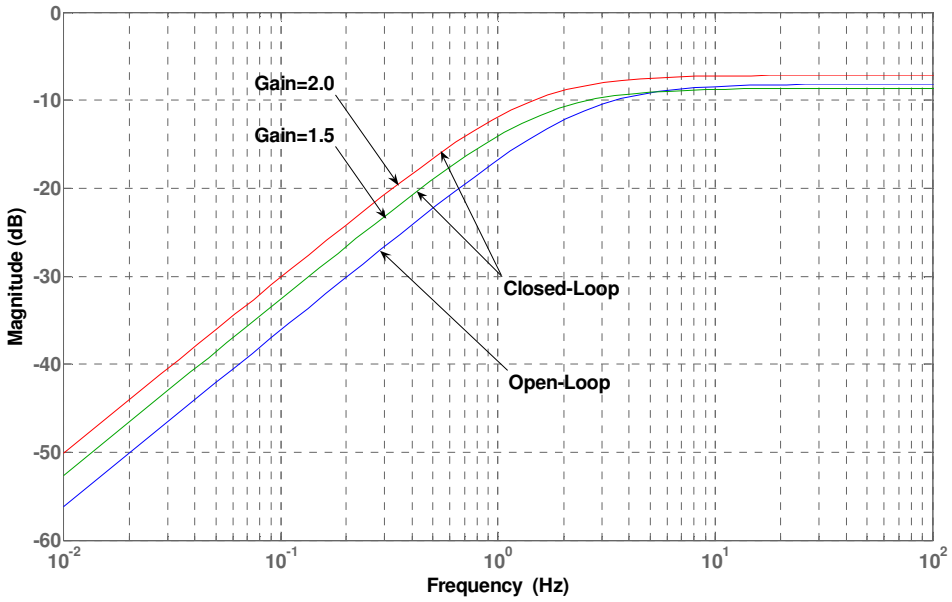


**Figure 3.10-** Magnitude frequency response $\left|\frac{\alpha_v(s)}{V_e(s)}\right|$ of the open-loop and closed-loop systems with proportional controller

Figure 3.10 indicates that the closed-loop control with proportional gain increased the bandwidth of the system, but only marginally improved the magnitude ratio. It should

be noted that in experiments, there was a limited room for increasing the proportional gain because of servovalve saturation.

Typical values of $K_{OL}$ and $\tau_o$ were extracted from the experimental frequency response of the actual system (Figure 3.6): $K_{OL} = 0.025\ s$ and $\tau_o = 0.064\ \ s$.

The ability of the system (open-loop and closed-loop) to follow the input was demonstrated in the time domain by inputting a 10 *Hz*. "joint vibration" (the output from the function generator) into the system. Figure 3.11 compares the responses of the open-loop and closed-loop models. It is evident that the closed-loop controller marginally increases the amplitude of the output acceleration when compared to the open-loop system. This is consistent with the gain increase in the frequency response shown in Figure 3.10 at 10 *Hz*. Increasing the gain eventually saturates the input signal to the servovalve and no further improvement was possible. It is clear that this is not an acceptable response.

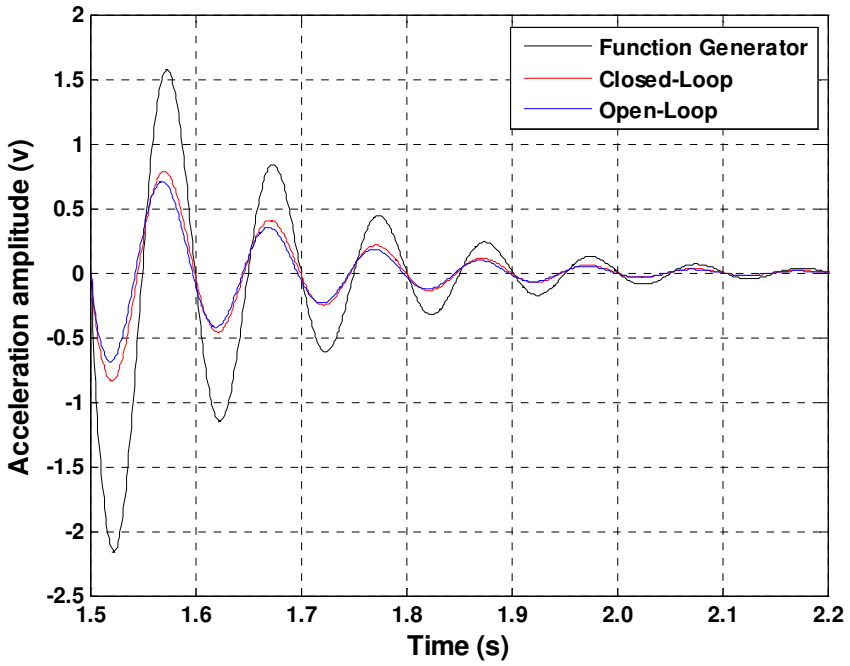


**Figure 3.11-** Transient response of $\alpha_v$ in the open-loop and closed-loop models with $K_P = 2$ to the function generator $\alpha_d$ of 10 *Hz* signal

A classical PI controller was then implemented. The closed-loop block diagram is shown in Figure 3.12.

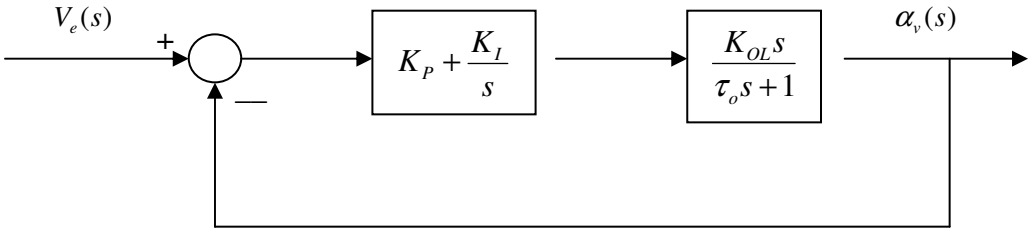


**Figure 3.12-** Block diagram of closed-loop control system with proportional and integral gains

In Figure 3.12;

$K_P$ proportional gain

$K_I$ integral gain $(1/s)$

The closed-loop transfer function in this case is derived with respect to the block diagram shown in Figure 3.12 as follows;

$$\left(\frac{\alpha_v(s)}{V_e(s)}\right)_{CL_2} = \frac{\dfrac{K_{OL}(K_P s + K_I)}{\tau_o s + 1}}{1 + \dfrac{K_{OL}(K_P s + K_I)}{\tau_o s + 1}}, \tag{3.17}$$

which is simplified to;

$$\left(\frac{\alpha_v(s)}{V_e(s)}\right)_{CL_2} = \frac{K_{OL}(K_P s + K_I)}{(K_P K_{OL} + \tau_o)s + (K_I K_{OL} + 1)}. \tag{3.18}$$

Using the same gain and time constant values as before,

i.e. $K_{OL} = 0.025\ s$ and $\tau_o = 0.064\ s$ , a comparison of the open-loop and closed-loop frequency responses (magnitude) for two controller gains is shown in Figure 3.13.

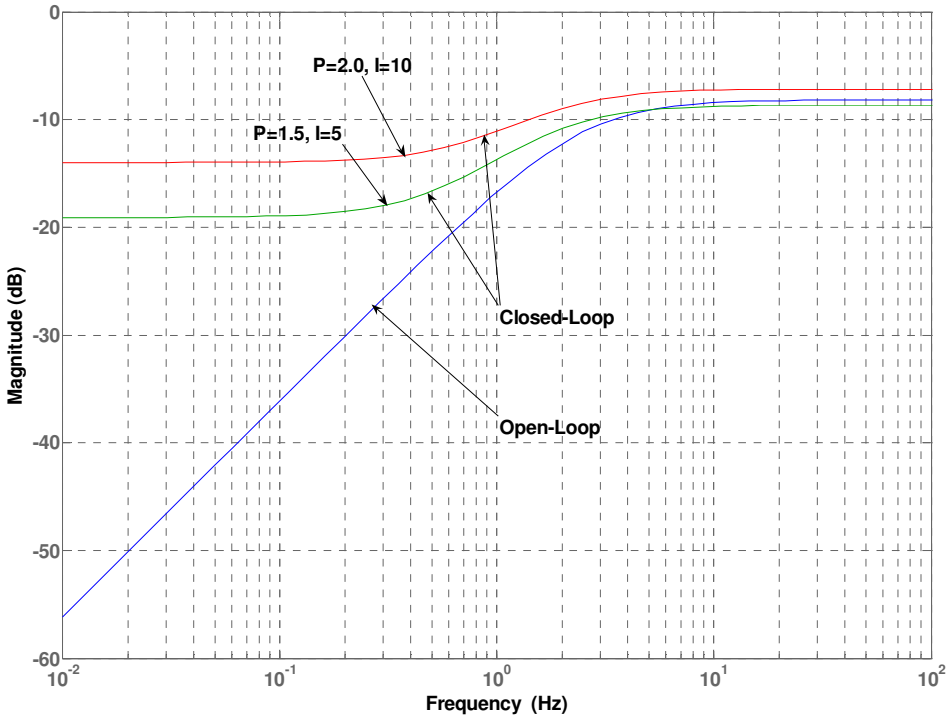


**Figure 3.13-** Magnitude frequency response $\left|\frac{\alpha_v(s)}{V_e(s)}\right|$ of open-loop and closed-loop systems with PI controller.

It can be observed from Figure 3.13 that the proposed PI controller could improve the response at lower frequencies better than the proportional controller, but the magnitude ratio was still a problem.

Figure 3.14 compares the time responses of the open-loop and closed-loop models for a 10 *Hz* joint function generator signal.

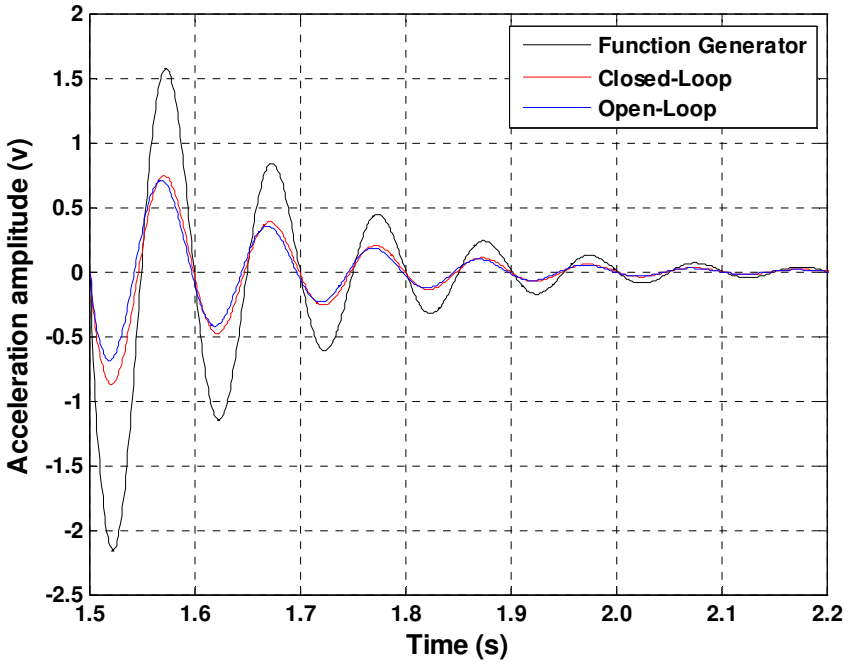


**Figure 3.14-** Transient response of $\alpha_v$ in the open-loop and closed-loop models with $K_P = 2$ and $K_I = 10$ to the function generator $\alpha_d$ of 10 $Hz$ signal

It is evident from Figure 3.14 that the PI controller also marginally improves that amplitude of the output but was not sufficient for the frequency range of interest in this study.

In Chapter 5 it will be shown that the P (proportional) or PI (proportional-integrator) closed-loop controllers could not be implemented physically because of noise in the accelerometer (sensor), significant nonlinearities in the rotary motor and high system internal gains. Therefore an alternate approach was proposed and is now considered.

### 3.3.2 Open-Loop Inverse Compensation Controller

To achieve the stated objective at the beginning of this section, a cascade compensator controller was proposed whose form was simply the inverse of the open-loop transfer function shown in equation 3.14. On the other hand, since the plant transfer function included a zero at the origin (Root-locus approach), the controller deemed to be an example of "marginally stable pole-zero cancellation" which might make the system unstable in some conditions (e.g. with constant disturbance or noise in the input signal). Therefore the controller pole was designed to be on the real axes, at the left hand side of imaginary axes and very close to the origin. This pole usually should be about $\varepsilon = 0.1/\tau_o$ away from the origin so that the magnifying signal does not exceed more than 10 times of the constant input noise. The block diagram of the controller is illustrated in Figure 3.15.

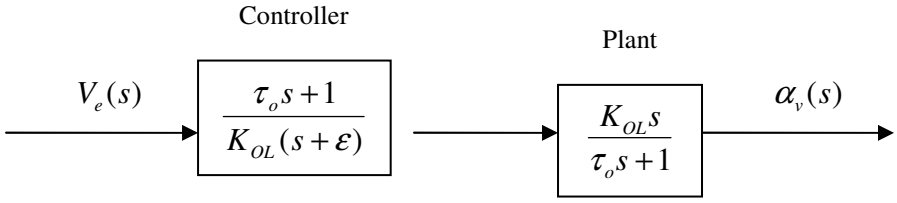


**Figure 3.15**- Block diagram of open-loop compensator controller

It should be noted that the open-loop pure inverse compensator which was proposed earlier might saturate the hydraulic simulator in frequencies lower than $\left|\frac{1}{\tau_o}\right|$ (2.5 *Hz* or 15.71 *rad/s* based on actual system magnitude Bode plot shown in Figure 3.6), however it was proved by simulation that the pure inverse controller worked properly in the frequency range of interest which was 5 to 15 *Hz*. Therefore $\varepsilon$ was set to zero and the controller was adopted to be in the form of $\frac{\tau_o s+1}{K_{OL}s}$. The transfer function of the system becomes $\left(\frac{\alpha_v(s)}{V_e(s)}\right)_{OL}$ = 1, which does meet the original objective. The controller must not

output a signal which would saturate the input to the hydraulic simulator. The form of the controller is quite ideal in that it inherently limits the input signal to the plant (assuming of course that the limit is less than saturation values). The disadvantage of this controller is that it is open-loop and any small drift in the plant input would be integrated twice by the plant resulting in substantial output position drift. To demonstrate the time response of the system with this inverse controller, the same signal from the function generator was input to the compensated servo system and as expected, the output acceleration follows the desired input signal perfectly. This is shown in Figure 3.16.

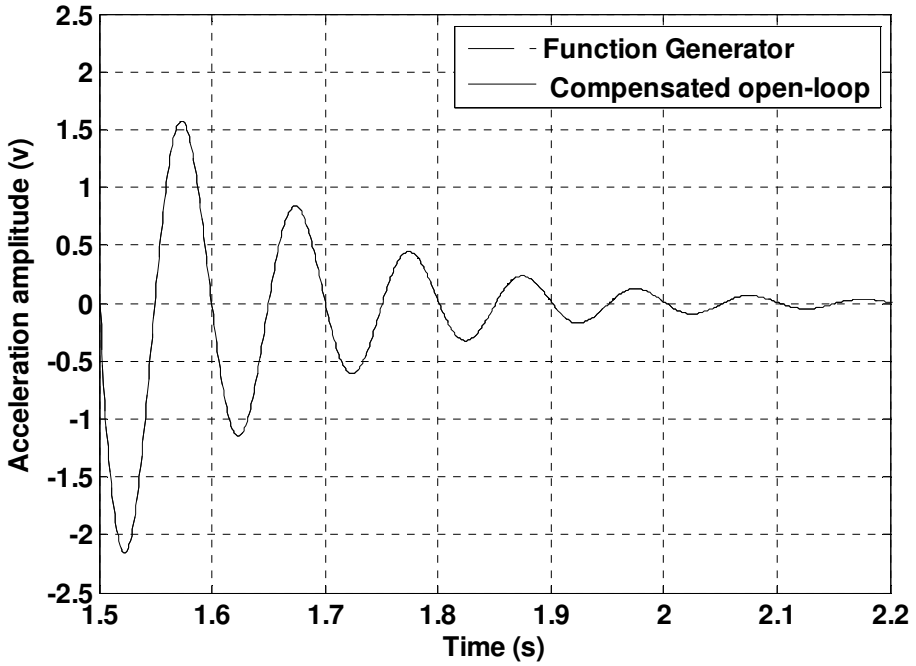


**Figure 3.16-** Transient response of $\alpha_v$ in the open-loop compensated model to the function generator $\alpha_d$ of 10 $Hz$ signal

# CHAPTER 4

# Experimental System Setup

## 4.1 Introduction

In Chapter 2, the development of the "function generator" was considered. In this chapter the experimental system (hydraulic simulator) setup is explained in detail. Figure 4.1 illustrates the schematic of the experimental system which includes the power supply, pressure servovalve, hydraulic rotary motor, and a single link manipulator.

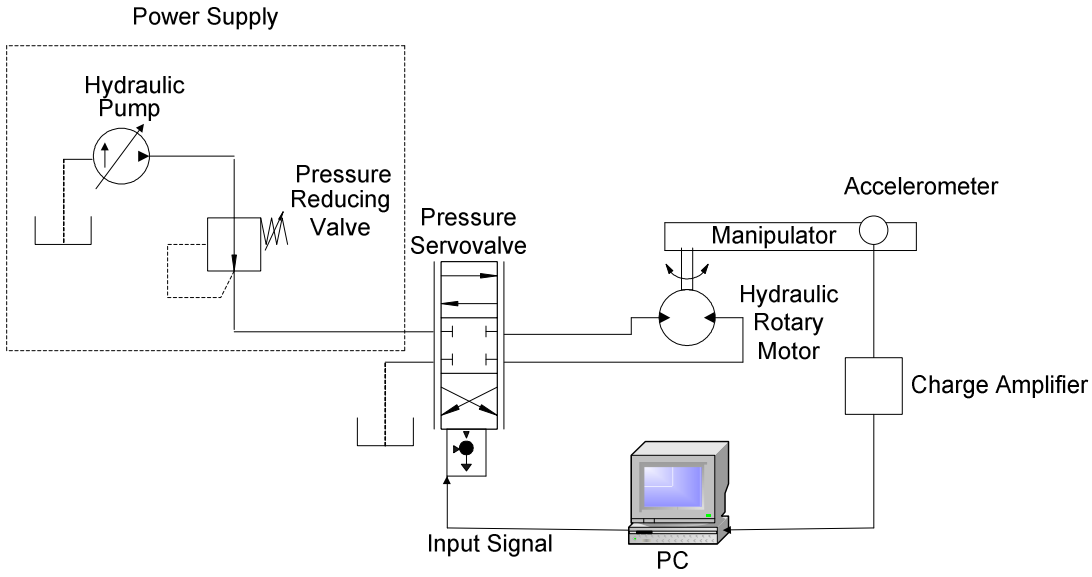


**Figure 4.1-** Schematic of the hydraulic simulator

The system was controlled by means of a personal computer using Matlab-Simulink software which submitted controlled input signals to the pressure servovalve. For analyzing the experimental system, a “Signal Analyzer Unit” was used. Also the angular acceleration of the link was measured by an accelerometer. In the following sections, each part and component is considered in detail.

### 4.2 Power Supply

The power supply consisted of a hydraulic pump and a pressure reducing valve. The hydraulic pump was a variable displacement, pressure compensated Sundstrand 22 series pump which delivered a maximum flow rate of 121.28 L/min. (32 GPM US) at 1740 RPM. The dead-head pressure of the pump was set at 172.5 bar (2500 psi). A Denison® model RR12535 pressure reducing valve limited the downstream system pressure to 86.25 bar (1250 psi).

### 4.3 Pressure Control Servovalve

As discussed in Chapter 3, a pressure servovalve was used because of its high frequency response, an important design criterion in this system. The Electrohydraulic, two-stage, four-way, nozzle-flapper type pressure control servovalve of Moog® model 15-010 was utilized to direct the flow from the power supply to the rotary motor. Figure 4.2 shows a schematic of the servovalve.

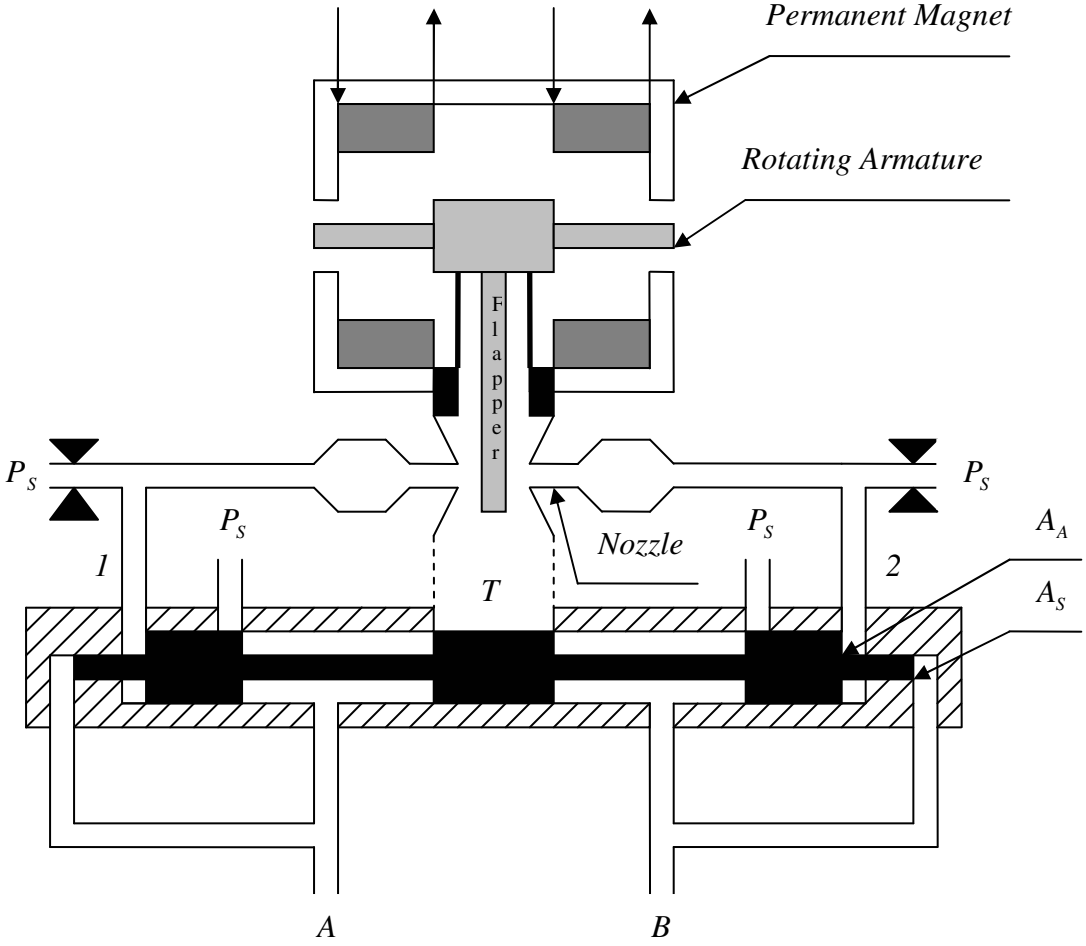


**Figure 4.2-** Schematic of pressure control servovalve

The servovalve consisted of three main parts: torque motor, hydraulic amplifier and valve spool assembly. This type of servovalve is designed to control load pressure difference ( $\Delta P_{AB}$ ). A summary of its operation is as follows.

The input current creates magnetic forces on the ends of the armature in the torque motor coils. This causes the armature and flapper assembly to rotate about a flexure tube support (not shown in Figure 4.2). The flapper moves between the nozzles and builds up a differential pressure $\Delta P_{12}$ which is proportional to torque created by the input current. The flapper restricts flow passing through one of the nozzles, for example nozzle (1) in Figure 4.2. Because of the fixed orifice upstream to the nozzle, a reduction in flow

results in an increase in the pressure just downstream of the fixed orifice which is sensed at the end of the spool (left hand side). Meanwhile, flow on the other side of the nozzle increases (wider opening and less restriction) which means that the pressure on the upstream side of the nozzle (downstream from the fixed orifice on the right hand side) decreases and is sensed by the right hand side of the spool. A pressure differential across the ends of the spool now exists and hence, the spool moves to the right (in this case). Fluid from the supply pressure ( $P_S$ ) is now ported to one control port and fluid in the second outlet is ported to the tank (*T*). As flow is ported to the load from $P_S$ , the pressure builds up (decreases on the other side of the actuator) and is fed back to the right hand side of the spool (the downstream side pressure is fed back to the left hand side of the spool). The load pressure difference ( $\Delta P_{AB}$ ) builds up a feedback force which eventually becomes equal to $\Delta P_{AB} \cdot A_S$ on the spool end. When $\Delta P_{AB} \cdot A_S = \Delta P_{12} \cdot A_A$ the spool stops moving and the output pressure differential is controlled. In Table 4.1 some specifications for the servovalve are presented [11].

**Table 4.1-** Specification of Moog servovalve model 15-010

| | |
|---|---|
| Input current | ±10.00 *ma* (rated) |
| Torque on Armature/Flapper | ±0.0100 $N \cdot m$ (rated) |
| Hydraulic Amplifier Flow to Drive the Spool | ±3.770 $cm^3 / s$ (max.) |
| Servovalve Flow, No-Load | ±902.0 $cm^3 / s$ (rated) |
| Spool Displacement | ±0.5080 *mm* (rated) |
| Hydraulic Amplifier Differential Pressure | ±61.41 *bar* (rated) |
| Load Differential Pressure | ±207.0 *bar* (rated) |
| Spool Driving Area | 26.45 $mm^2$ |
| Spool Feedback End Area | 7.871 $mm^2$ |

A pressure servovalve was chosen because of its high cutoff frequency characteristics and the fact that relatively small flow rates were required. The servovalve was installed as close as possible to the rotary motor in order to minimize the effects of compressibility of the hydraulic fluid and to maximize the stiffness of the system by reducing the volume of fluid (load side).

### 4.4 Hydraulic Rotary Motor

A single vane hydraulic rotary motor (Micromatic® model MPJ-22-1V) was used as the actuator. Table 4.2 illustrates some specification of this motor [12].

**Table 4.2-** Specifications of Micromatic rotary motor MPJ-22-1V

| | |
|---|---|
| Torque $(N \cdot m)$ | 6.330 @ 6.90 bar |
| | 37.63 @ 34.5 bar |
| | 76.73 @69.0 bar |
| Volumetric Displacement $(cm^3)$ | 62.61 *per* 270º |
| | 13.36 *per radian* |
| Max. Operating Pressure (*bar*) | 69.00 |
| Max. Rotating Angle | 270.0º |

As will be presented in Chapter 5, this rotary motor displayed significant nonlinear characteristics. Since it was the only one available in the laboratory, it had to be used. This certainly posed some interesting challenges for the controller design.

### 4.5 Robot Manipulator

The original manipulator used in this research project was designed, constructed and reported in a thesis entitled “Planar Manipulator with Three Revolute Joints” [13]. The schematic front view is shown in Figure 4.3 and a photo is shown in Figure 4.4. Some modifications were made to the original manipulator to prepare it for the purpose of the project. This was a two-degree-of-freedom rigid link manipulator, which included two hydraulic rotary motors at the shoulder and elbow joints, and two rigid shoulder and elbow links. Due to the fact that the “shoulder” actuator (a Char-Lynn series 2000) was a disc valve type rotary motor with significant viscous friction and a narrow range of motion (180º), the decision was made not to use this actuator. Instead, the elbow actuator was used which had less viscous friction and a wider range of motion (270º). To stabilize the manipulator, the shoulder link was fixed and secured by utilizing a number of cables and plates with bolts and nuts. The wrist actuator was subsequently used as a load at the end of the elbow link. Figure 4.3 illustrates the schematic of the manipulator.

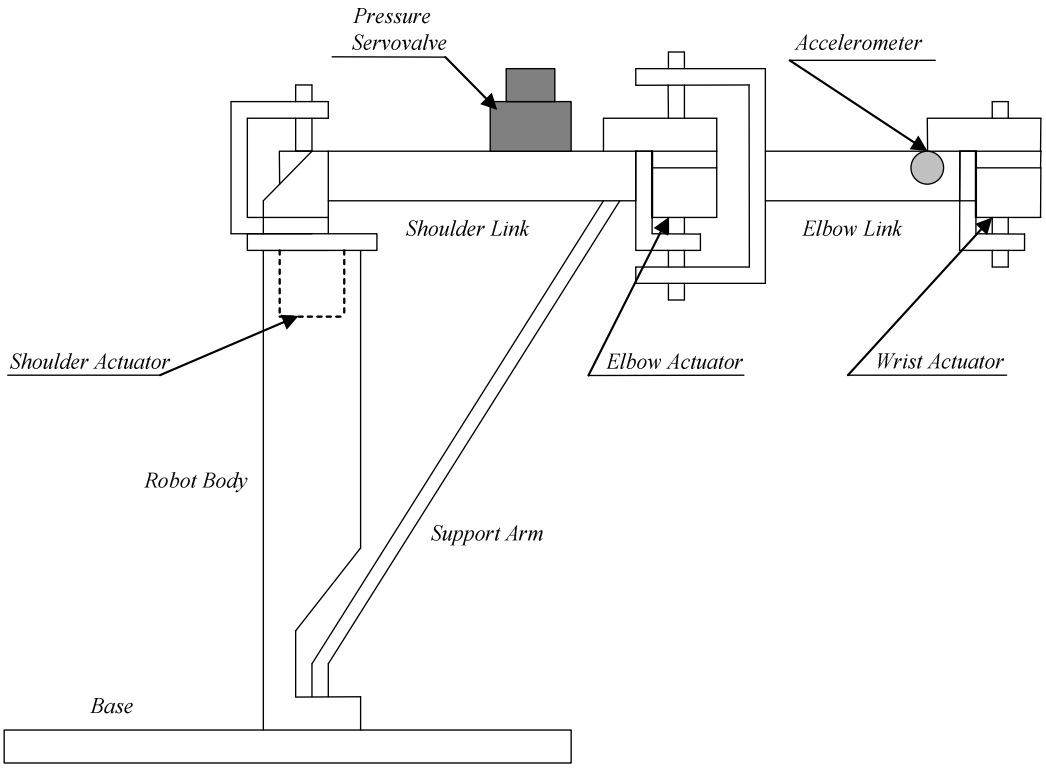


**Figure 4.3-** Schematic of the two-link rigid manipulator in which the shoulder link was fixed

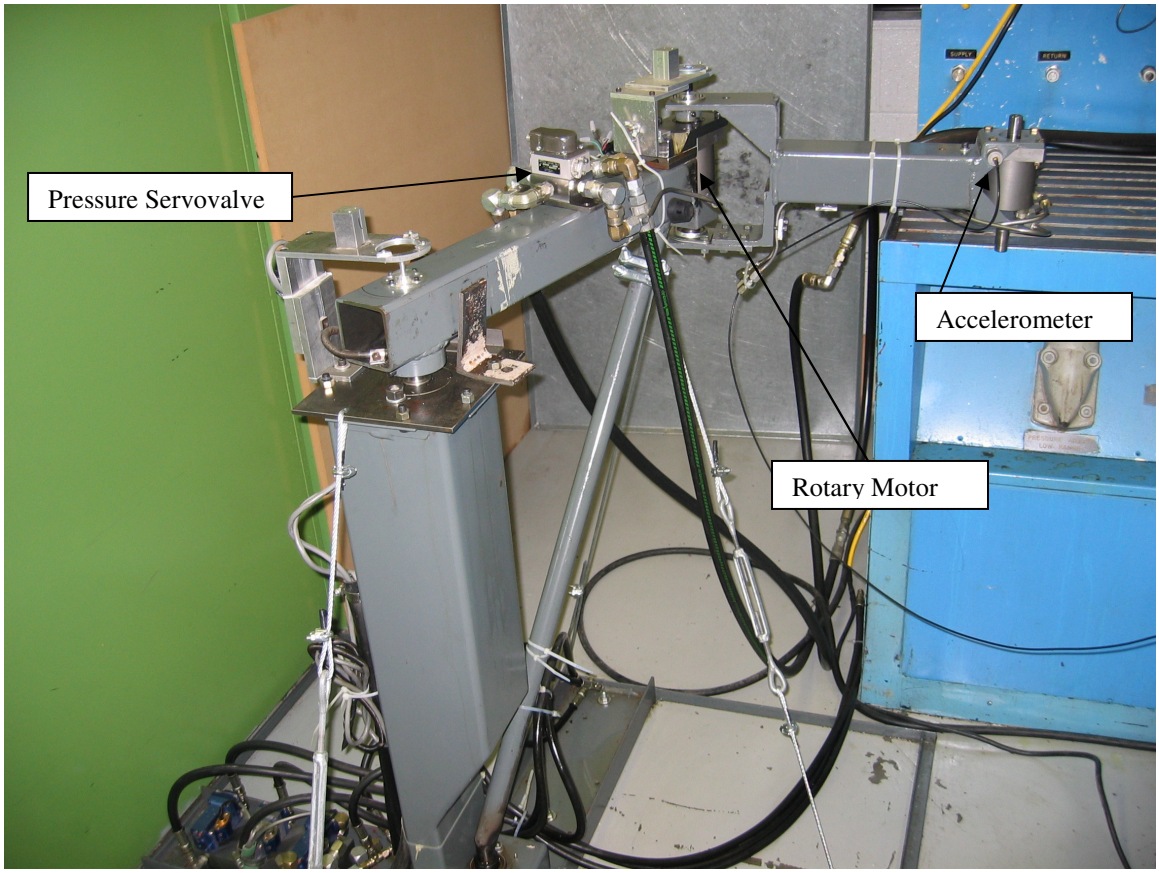


**Figure 4.4-** Photo of the manipulator setup used in the experiment

The pressure control servovalve was installed at the top of the fixed shoulder link which was the shortest distance to the operating actuator (elbow actuator) to minimize the compressibility effect of the hydraulic fluid.

Table 4.3 lists some particulars of the manipulator [13]. As indicated in the Table 4.3, the construction of the robot manipulator was strong enough to be considered as a rigid manipulator.

**Table 4.3-** Important manipulator measurements

| | |
|---|---|
| Shoulder link length | 0.6100 *m* |
| Shoulder link cross section | 0.0760 *m* square steel tube<br>0.0060 *m* wall thickness |
| Elbow link length | 0.4600 *m* |
| Elbow link cross section | 0.0750 *m* square steel tube<br>0.0050 *m* wall thickness |
| Shoulder link weight<br>(without servovalve) | 15.90 *kg* |
| Elbow link weight | 8.600 *kg* |

## 4.6 Personal Computer

In addition to using a personal computer with Matlab-Simulink Real Time Windows Target for software algorithm programming, a National Instruments PCI-6025e data acquisition card with a 12bit A/D and D/A was used to interface the input signal from the computer to the servovalve and the accelerometer signal back to the computer. The "function generator" in the Simulink program was utilized to provide the input signal to the "hydraulic simulator". Table 4.4 presents some the pertinent settings that were used in the Matlab-Simulink algorithm.

**Table 4.4-** Matlab-Simulink setup for experimental system control

| | |
|---|---|
| Solver Type | Fixed-step |
| Solver | ode4 (Runge-Kutta) |
| Fixed-Step Size (Fundamental Sample Time) | 0.001 s |
| Analog input | National Instruments® PCI-6025E (auto), input range ±10 v |
| Analog output | National Instruments® PCI-6025E (auto), output range ±10 v |

## 4.7 Signal Analyzer

A signal analyzer unit (Bruel & Kjaer® type 2035) was used to obtain the frequency response data of the system. The analyzer provided the actual Bode magnitude and phase plots of the experimental system.

The analyzer generates a random signal of various frequencies ranging from 0 *Hz* to 200 *Hz* (for this test). Other frequency ranges were possible with this unit. The signal was interfaced to the servovalve via one channel as the system input signal. The measured acceleration (output signal) was returned to the analyzer via another channel.

### 4.8 Accelerometer

A piezoelectric charge accelerometer of Bruel & Kjaer® type 4370 was attached to the linkage (see Figures 4.3 and 4.4). The accelerometer was connected to a charge amplifier of Bruel & Kjaer type 2635. The calibrated output rating of the charge amplifier was adjusted to $0.1(\frac{v}{m/s^2})$.

The accelerometer was capable of measuring tangential acceleration. However, it was the angular acceleration that was desired. Since the distance between the center of the installed accelerometer and the vertical axis of the rotary motor (rotation arm) was known, it was possible to convert the linear (tangential) acceleration to angular acceleration (details were provided in Chapter 3).

### 4.9 Accelerometer Compensator

In Chapter 3 it was mentioned that the actual frequency response of the experimental system, shown in Figure 3.6, was best approximated by the theoretical frequency response illustrated in Figure 3.4. In reality, the slope of the actual Bode plot (Figure 3.6) was greater than the theoretical plot at low frequencies. It was believed that the poor performance of the accelerometer and amplifier at low frequencies was a possible reason for this discrepancy. Upon further testing, (as follows) it was determined that the accelerometer/amplifier displayed the characteristics of a high-pass filter.

An accelerometer test was performed on a “shaker table” utilizing an accurate linear position sensor (Schaevitz® DCLVDT) along with the test accelerometer (B&K 4370) which were both installed on the same plane of motion. The random signal generated by the signal analyzer was interfaced to the shaker table. The output signal of the position transducer was connected to the analyzer. The analyzer was set to convert the position

signal to an acceleration signal by differentiating it twice. The output signal of the test accelerometer was also interfaced to the analyzer. The analyzer was utilized to compare amplitude and phase angle of acceleration (derived from the position signal) with those of the test accelerometer signal. Figure 4.5 illustrates the schematic of the test arrangement.

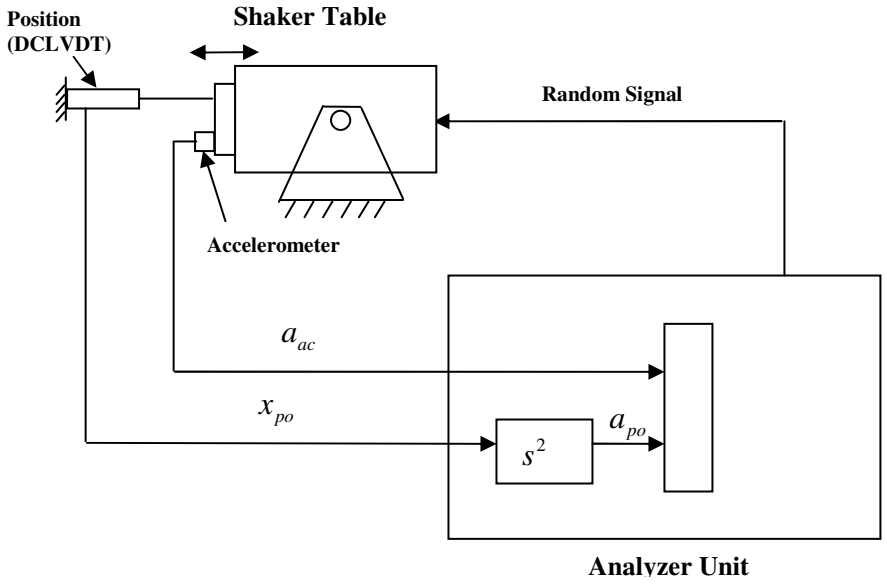


**Figure 4.5-** Schematic of "Shaker Table" test

In Figure 4.5;

$a_{ac}$ measured accelerometer's acceleration $(v)$

$x_{po}$ measured position $(v)$

$a_{po}$ calculated acceleration by double differentiation of measured position $(v)$

Figure 4.6 shows the magnitude and phase Bode diagram of twice differentiated position signal and the test accelerometer signal.

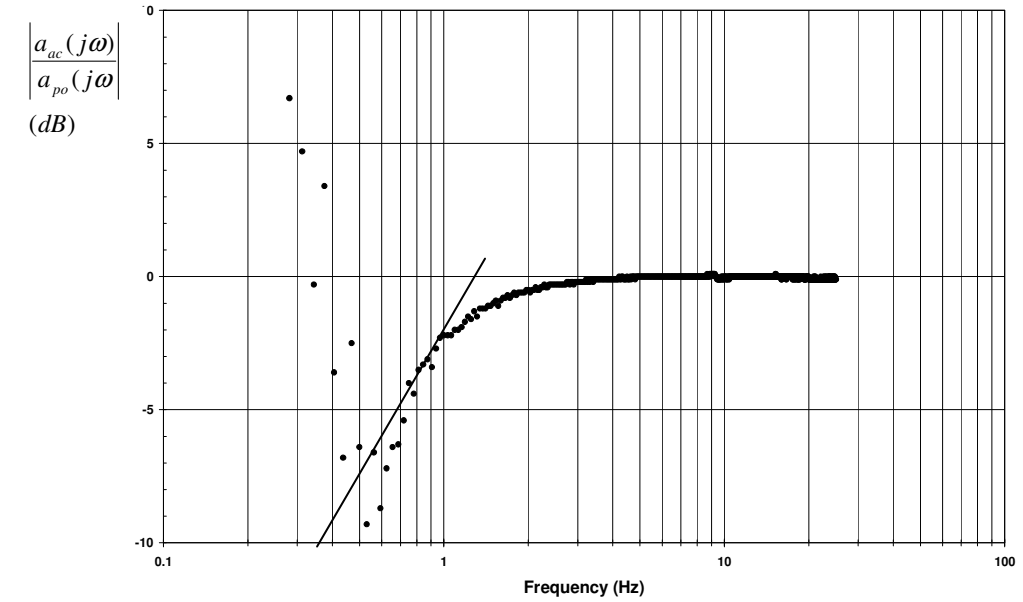


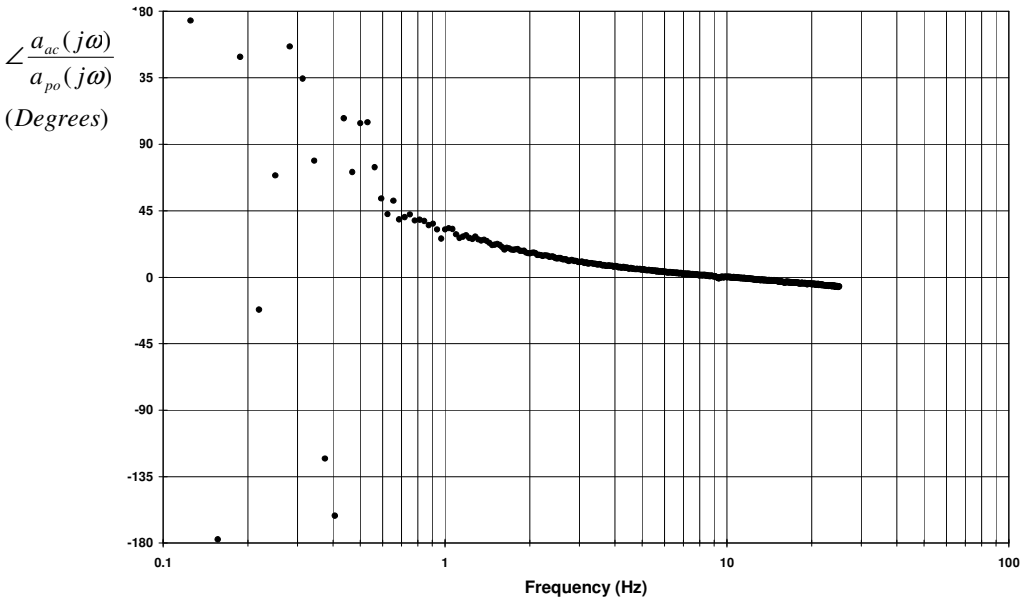


**Figure 4.6-** Magnitude and phase Bode plots of the shaker table test (points are data from the analyzer and the solid line is the straight line approximation based on a 20 dB per decade slope).

An approximated transfer function of the two acceleration signals can be extracted from an asymptotic analysis of the magnitude Bode plot which is shown in Figure 4.6. It is evident that at low frequencies, the accelerometer produced results which were attenuated. This attenuation could be approximated by a transfer function. Analysis of Figure 4.6 indicates that the corner frequency was 1.25 *Hz* (7.85 *rad/s*). Therefore the transfer function which reflected this low frequency attenuation was estimated to be;

$$G_{ac} = \frac{s}{s + 7.85} \tag{4.1}$$

To compensate for this attenuation, a compensator was chosen to be $\frac{s + 7.85}{s + 5.00}$ in order to expand the lower end of bandwidth of the accelerometer.

It should be noted that an ideal compensator should be $\frac{s + 7.85}{s}$ but as will be discussed in Chapter 5, the form $\frac{s + 7.85}{s + 5.00}$ provided better compensation. More details will be discussed on this matter in the following chapter in which experimental data is considered.

In implementing this accelerometer compensator experimentally, the proposed compensator was installed after the plant and physical accelerometer. Figure 4.7 illustrates the placement of the compensator to a theoretical approximation of the accelerometer frequency characteristics. Chapter 5 will consider the implementation of the compensator from an experimental point of view.

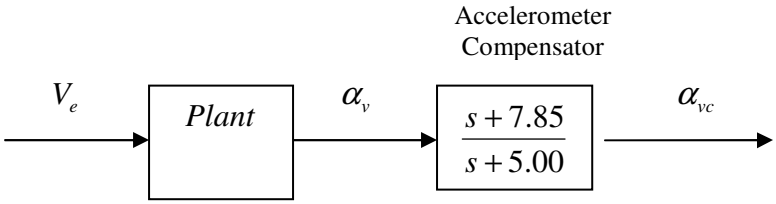


**Figure 4.7-** Block diagram of the system with the accelerometer compensator

It should be noted that this compensator was utilized for all experimental tests.

# CHAPTER 5

# EXPERIMENTAL RESULTS

## 5.1 Introduction

The objective of this chapter is to present and discuss the results of the tests performed on the experimental system with the setup explained in Chapter 4. Generally, the tests made use of "swept" frequencies (a process in which the input frequency was systematically increased over a selected frequency range) and function generator inputs to produce both frequency and time domain results. For many of the tests, magnitude and phase Bode diagrams were developed from the data to illustrate the dynamic performance of the system and compensation schemes. To demonstrate the desired use of the hydraulic simulator, the temporal responses to the output from the function generator were considered. The Chapter will then illustrate the transient response tracking errors and "mean squared error" values.

## 5.2 Pressure Control Servovalve

The pressure control servovalve was used in the hydraulic simulator because of its superior frequency bandwidth at low flow rates when compared to a flow control servovalve [14]. The pressure control servovalve dynamic performance (the frequency response data) is generally presented in two forms; one in which the load ports of the

servovalve are blocked (blocked load) and the other when the ports are connected to a load. The blocked load test is normally conduced by "plugging" the load ports (for example ports A and B in Figure 4.2). The load pressure difference ( $\Delta P_{AB}$ ) and the input voltage are measured for a wide range of sinusoidal frequencies (in the following case between 0.5 to 400 $Hz$). In the blocked load case the servovalve should demonstrate a high stiffness because of the very small fluid volume on the load side resulting in a higher natural frequency.

Figures 5.1a and b illustrate the relationship of blocked load differential pressure to input voltage to the servo-amplifier. As can be observed in the Bode plot, the bandwidth of the valve was approximately zero to 60 $Hz$ which was somewhat less than that stated in the manufacturer's specifications [11]. At higher frequencies, a slope of -60dB/decade in the magnitude plot indicated that the system was approximately third-order.

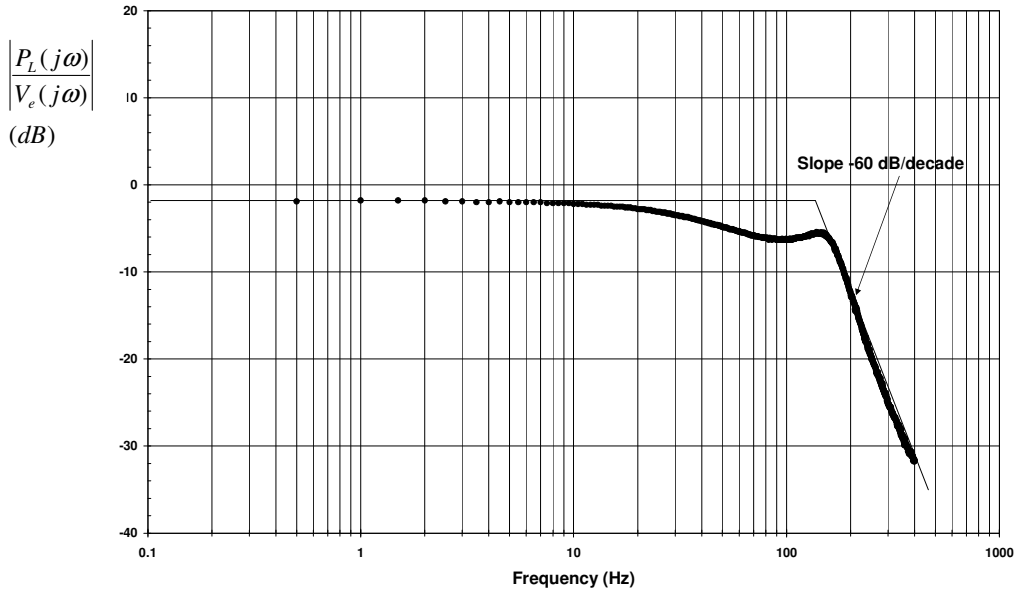


**Figure 5.1a–** Magnitude frequency response of the pressure control servovalve with a blocked load (points are data from the analyzer and the solid line is the straight line approximation).

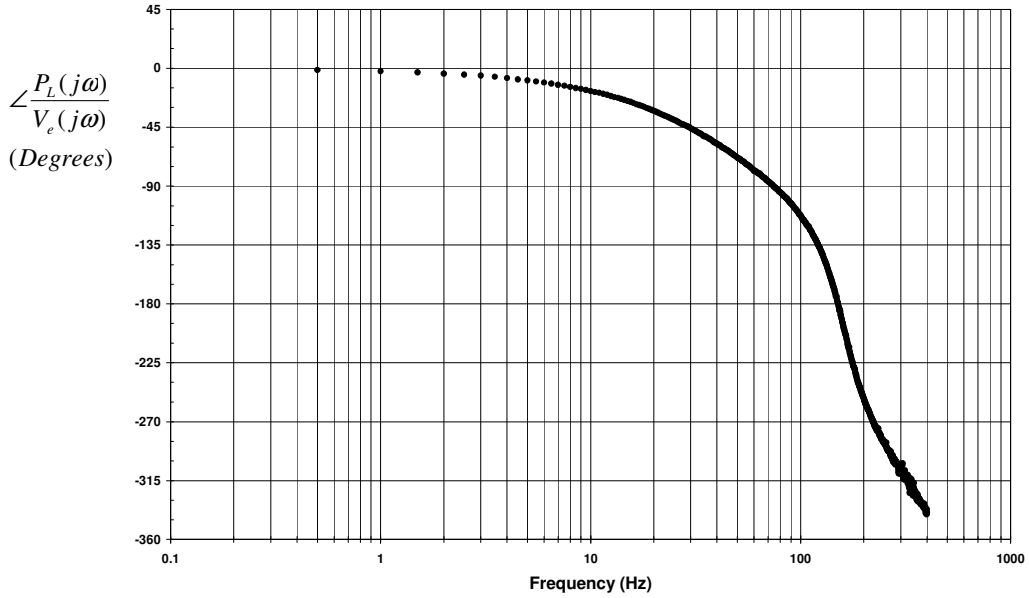


**Figure 5.1b–** Phase frequency response of the pressure control servovalve with a blocked load.

When the pressure control servovalve was connected to the experimental system, the frequency response was determined and is shown in Figures 5.2a and b.

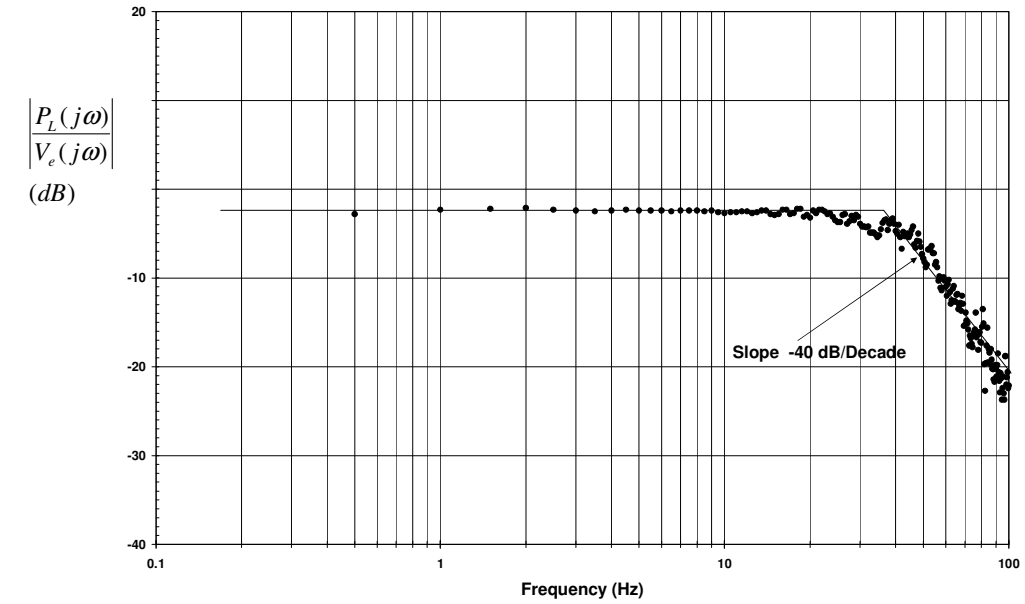


**Figure 5.2a-** Magnitude frequency response of pressure control servovalve with actual hydraulic simulator load (points are data from the analyzer and the solid line is the straight line approximation).

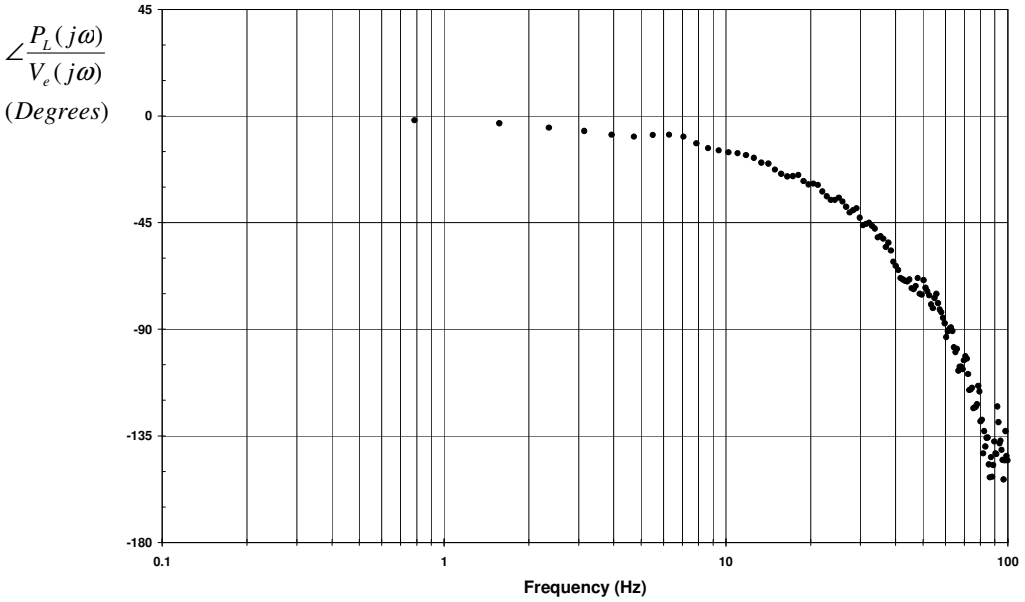


**Figure 5.2b-** Phase frequency response of pressure control servovalve with actual hydraulic simulator load.

It is observed that the bandwidth is about 40 *Hz* and the order of the system has changed from third to second. The influence of the load is thus apparent. The high frequency affects of the servo-amplifier are not visible from these results and hence the assumption that the servo-amplifier could be approximated by a simple gain in Chapter 3 was justified.

The frequency response of the actual load pressure to input voltage (Figure 5.2a and b) demonstrates that the selected pressure control servovalve was capable of an appropriate performance in the frequency range of interest (5-15 *Hz*).

### 5.3 Accelerometer

In Chapter 4 it was stated that the accelerometer was demonstrating poor performance at the lower frequencies. It was believed that some method of calibrating the accelerator at low frequencies was necessary. As discussed in Chapter 4, a "shaker table" test facility was available in the laboratory which could be used to provide a calibrated position measurement and hence a reliable acceleration calculation. Both the accelerometer and position transducer were mounted on the table and the shaker table frequency range swept from 1 to 25 *Hz*. The "calibrated" acceleration was determined by a double differentiation of the position signal. The magnitude and phase ratio of the accelerometer $a_{ac}$ output to the calculated acceleration $a_{po}$ from the position transducer were shown in Figure 4.6. Ideally the magnitude ratio should be unity and the phase shift zero. Observation of Figure 4.6 illustrates that the performance of the accelerometer deteriorates at frequencies less than 7.85 rad/s (1.25 *Hz*).

As discussed in Chapter 4, an ideal compensator of the form $G_1 = \frac{s + 7.85}{s}$ should extend the lower frequency range of the accelerometer. When applied to the actual system, the results were not satisfactory in that the compensator "overcompensated" the accelerometer's signals at frequencies below 7.85 rad/s (1.25 *Hz*). The assumption that

the actual data followed the transfer function $G_1$ is only approximate in that the slopes are comparable but in the transition regions between the two slopes, the experiential data was found to be larger than that predicted by the transfer function $G_1$. Thus data in that region was amplified beyond that required; thus overcompensated. In addition, the data for frequencies less than 1 *Hz* was very erratic and the use of $G_1$ would only amplify the scatter at lower frequencies (see Figure 4.6). Thus a compensator of the form $\frac{s+a}{s+b}$ which would not amplify the lower frequencies but compensate at the break point was used. This compensator was tuned to be in the form of $\frac{s+7.85}{s+5.00}$ which was then applied to all measured acceleration data.

Figures 5.3a and b indicate the relationship between the accelerometer output signal and double differentiated signal from the position transducer, with the proposed compensator. A comparison of Figure 5.3 to Figure 4.6 in Chapter 4 shows that the lower end of bandwidth of the accelerometer has been extended from 3 *Hz* to about 1 *Hz*. However, there is still a slight affect on the amplitude ratio in the range from 1 to 10 *Hz*, which is not desirable. The overall improvement using this compensator was considered marginal but was still implemented in all subsequent studies.

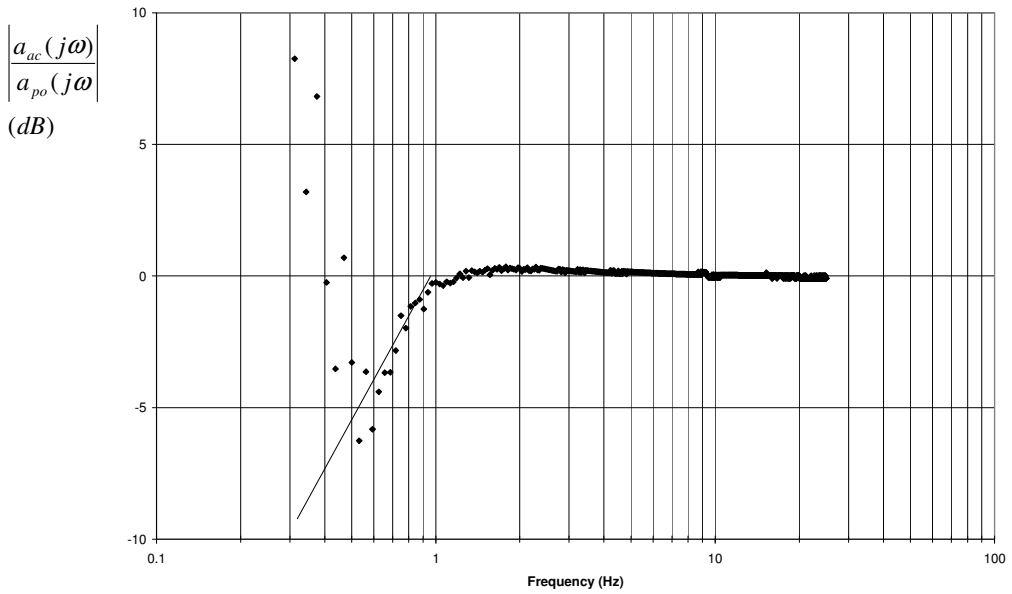


**Figure 5.3a-** Magnitude ratio $\left|\frac{a_{ac}(j\omega)}{a_{po}(j\omega}\right|$ versus frequency of the accelerometer with proposed accelerometer compensator (points are data from the analyzer and the solid line is the straight line approximation).

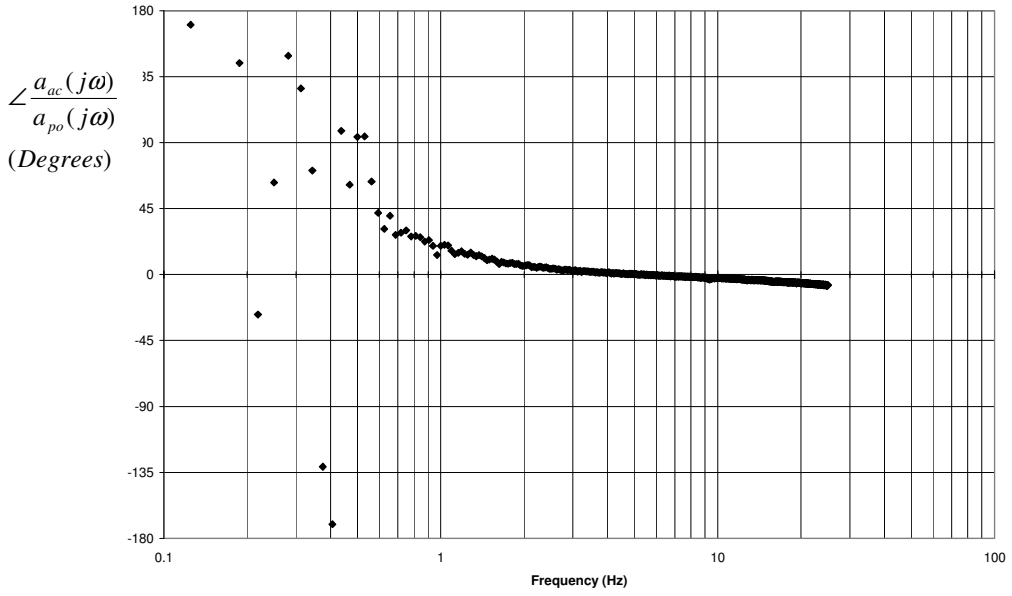


**Figure 5.3b-** Phase $\angle\frac{a_{ac}(j\omega)}{a_{po}(j\omega)}$ versus frequency of the accelerometer with proposed accelerometer compensator.

The compensator was then applied to the acceleration data from the hydraulic simulator and the dynamic performance (magnitude wise only) before and after compensation is compared in Figures 5.4 and 5.5. It is apparent that in the lower frequency range (less than 2 *Hz*), the slope of the frequency response after applying the compensator is now 20 db per decade which is consistent with what was predicted from the theoretical model of the system (Chapter 3). However, consistent with the "overcompensating" nature of the accelerometer in the frequency range of 1 to 10 *Hz*, there appears some distortion to the frequency response in the plant data as well. However, because in the lower frequency range, the slope with the compensated accelerometer approached that which was predicted analytically, it was concluded that the accelerometer compensation was acceptable for this study.

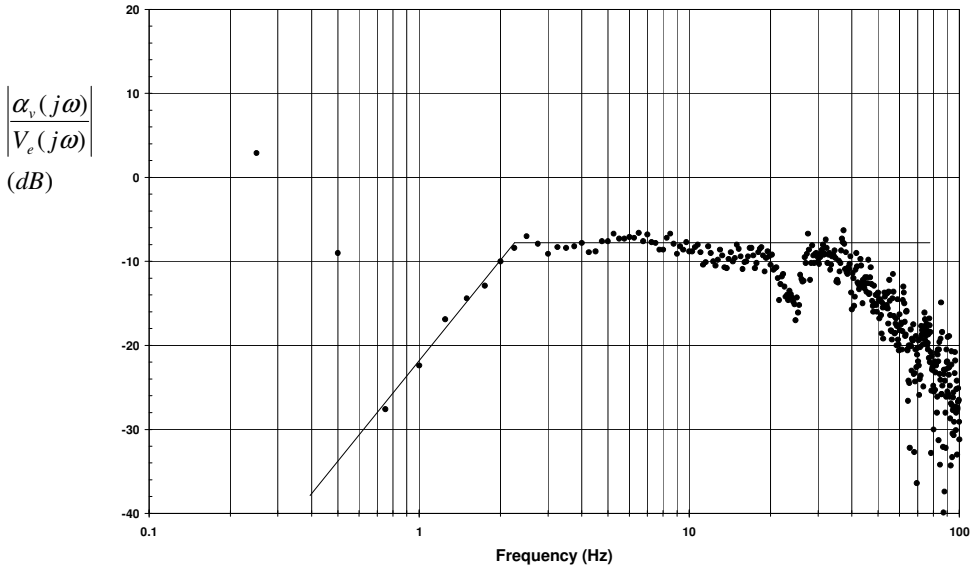


**Figure 5.4-** Open-loop magnitude frequency response of the hydraulic simulator before applying the accelerometer compensator (points are data from the analyzer and the solid line is the best fit straight line approximation; 40 dB per decade slope).

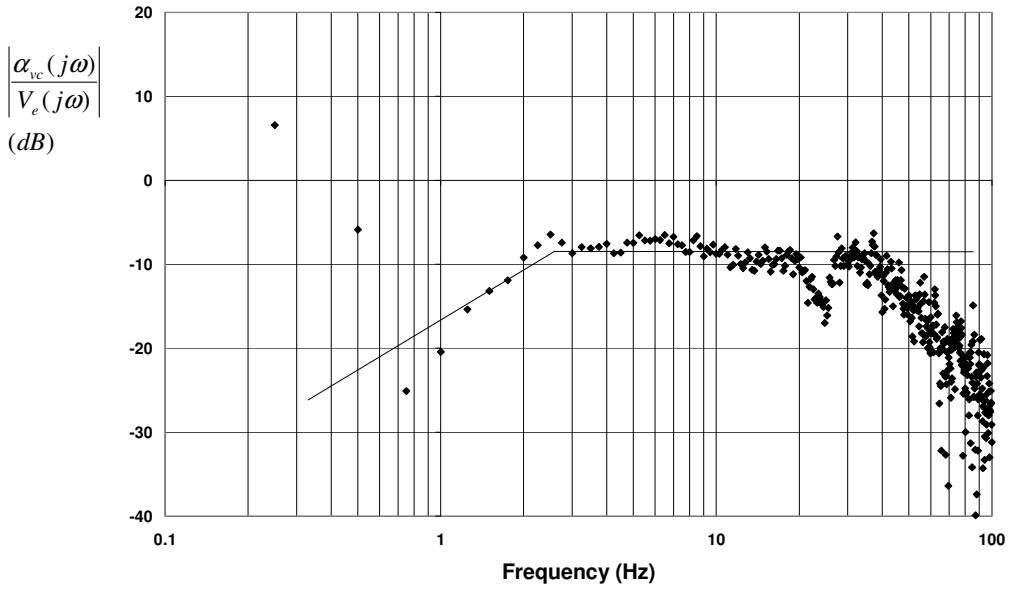


**Figure 5.5-** Open-loop magnitude frequency response of the hydraulic simulator after applying accelerometer compensator (points are data from the analyzer and the solid line is the expected straight line approximation of the plant, 20 dB per decade slope).

## 5.4 Hydraulic Simulator

The experimental results of the "hydraulic simulator" such as open-loop and closed-loop frequency responses, open-loop compensated frequency response, open-loop transient responses and transient response errors are presented and discussed in this section.

### 5.4.1 Open-Loop Frequency Responses

The open-loop behavior of the hydraulic simulator is shown in Figure 5.5. It is observed that the gain is -8 dB and has a bandwidth of approximately 2 to 30 *Hz*. An unknown dip in the magnitude occurs at 25 *Hz*; at this point no reasonable explanation can be forwarded for this behavior.

The frequency response of the open-loop hydraulic simulator for smaller input amplitudes of $0.5v$ (a small acceleration of 11.5 $rad/s^2$) is shown in Figure 5.6a and b. It is evident that the performance deteriorates in that the lower cutoff frequency is increased to 5 *Hz* and the magnitude dips at 25 *Hz* significantly. The performance continues to deteriorate significantly as the input voltage (desired acceleration) decreases to $0.1v$ ( 2.3 $rad/s^2$ ). The frequency response at $0.1v$ ( 2.3 $rad/s^2$ ) is shown in Figures 5.7a and b. It is clear that the presence of some nonlinear phenomenon has a significant effect on the frequency response. The importance of this result will be seen in the acceleration transient responses, especially at small input amplitudes. These results will have an effect on the open-loop cascade compensator that was proposed in Chapter 3.

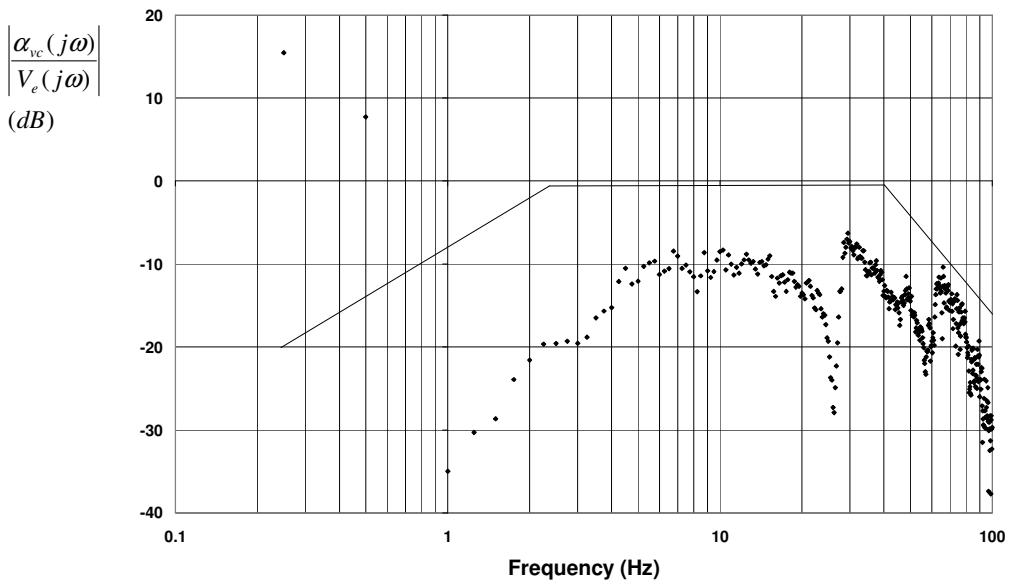


**Figure 5.6a-** Open-loop magnitude frequency response of the hydraulic simulator with input amplitude of 0.5*v* or 11.5 $rad/s^2$ (solid line is the ideal theoretical frequency response).

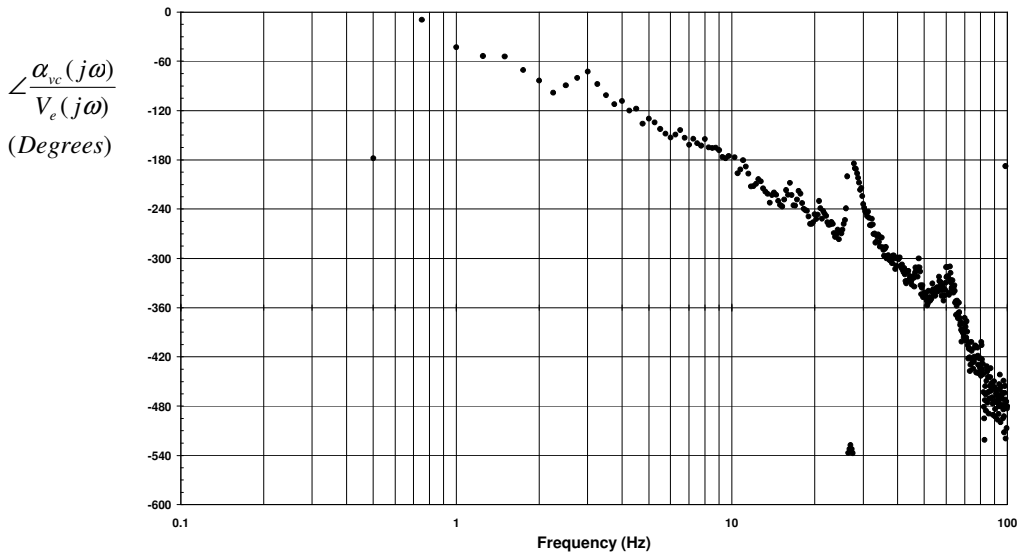


**Figure 5.6b-** Open-loop phase frequency response of the hydraulic simulator with input amplitude of 0.5*v* (11.5 $rad/s^2$)

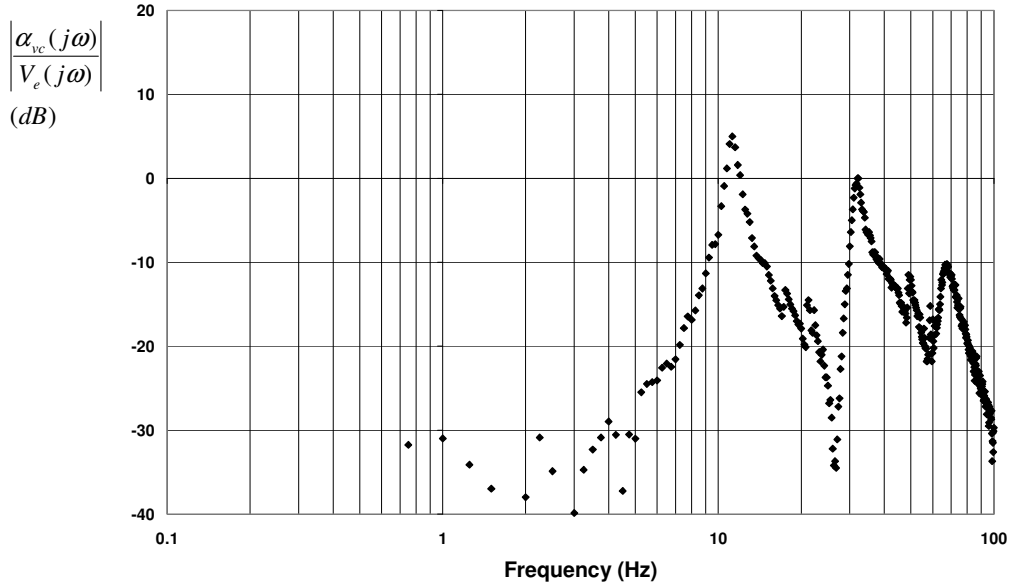


**Figure 5.7a-** Open-loop magnitude frequency response of the hydraulic simulator with input amplitude of $0.1v$ ( $2.3\ rad/s^2$ )

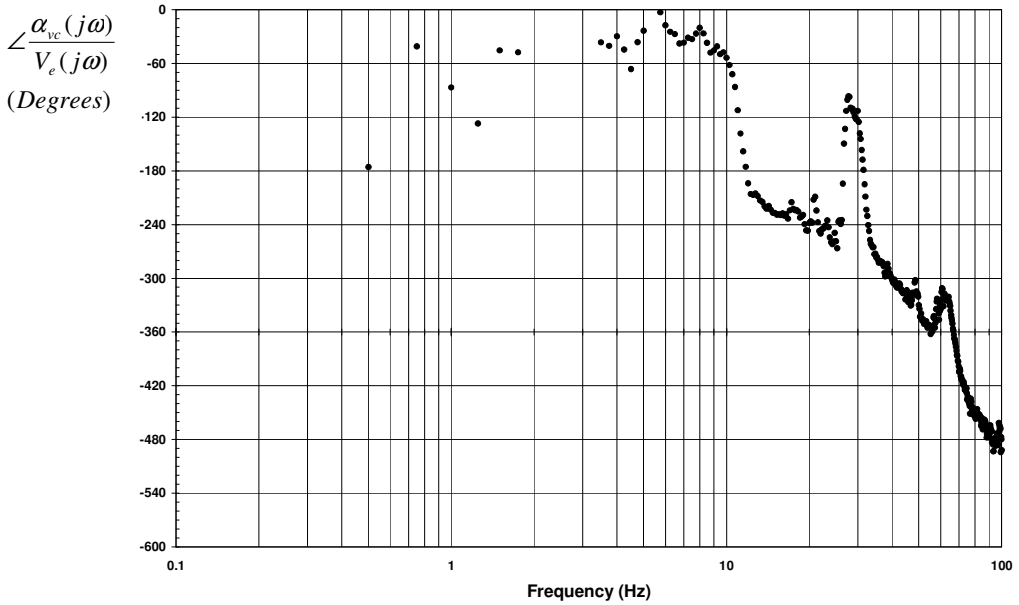


**Figure 5.7b-** Open-loop phase frequency response of the hydraulic simulator with input amplitude of $0.1v$ ( $2.3\ rad/s^2$ )

### 5.4.2 Closed-Loop Frequency Responses

It was of interest to apply a closed-loop proportional control system to demonstrate the results predicted in Chapter 3. Figure 5.8 indicates the closed-loop dynamics (magnitude Bode plot only) of the hydraulic simulator. The gain is -10dB which means the amplitude ratio of 1 (0dB) was not achieved as predicted by theory in Chapter 3. There was however, a marginal improvement in the bandwidth at lower frequencies. What this would translate to in the transient response studies is that the amplitude of the output waveform would be attenuated compared to the desired waveform. The input amplitude of the desired acceleration was $1v$ ( $23.0\ rad/s^2$ ).

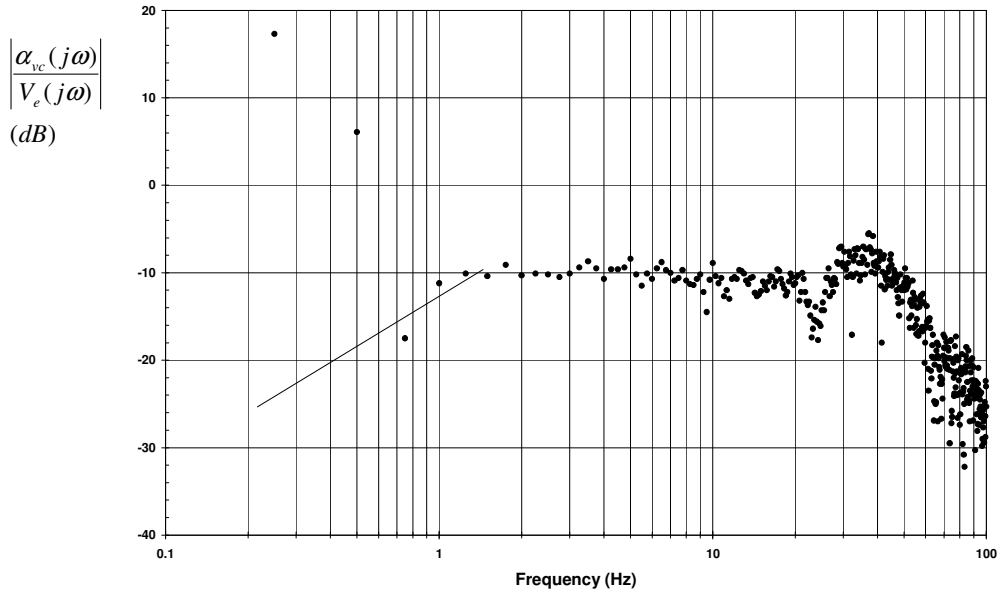


**Figure 5.8-** Closed-loop magnitude frequency response of the hydraulic simulator with input amplitude $1.0v$ or $23.0\ rad/s^2$ (points are data from the analyzer and the solid line is the straight line approximation, 20 dB per decade).

The closed-loop frequency response of the hydraulic simulator at input amplitudes of $0.5v$ ($11.5 rad/s^2$) and $0.1v$ ($2.3\ rad/s^2$) are shown in Figures 5.9 and 5.10 (magnitude

only). Similar to the open-loop results, the dynamic performance of the closed-loop frequency responses deteriorates significantly as the amplitude of input signal decreases.

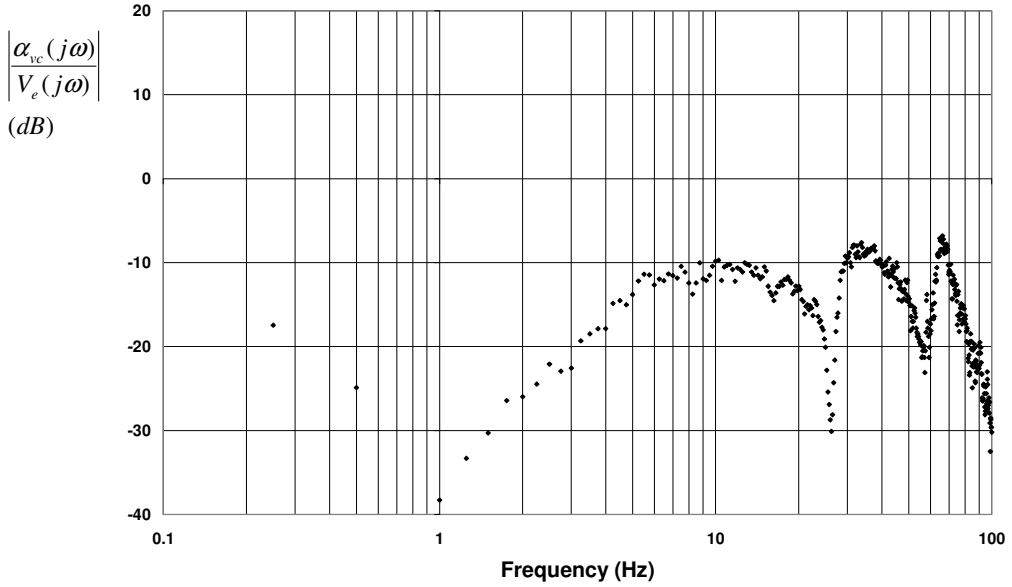


**Figure 5.9-** Closed-loop magnitude frequency response of the hydraulic simulator (input amplitude $0.5v$ or $11.5\ rad/s^2$).

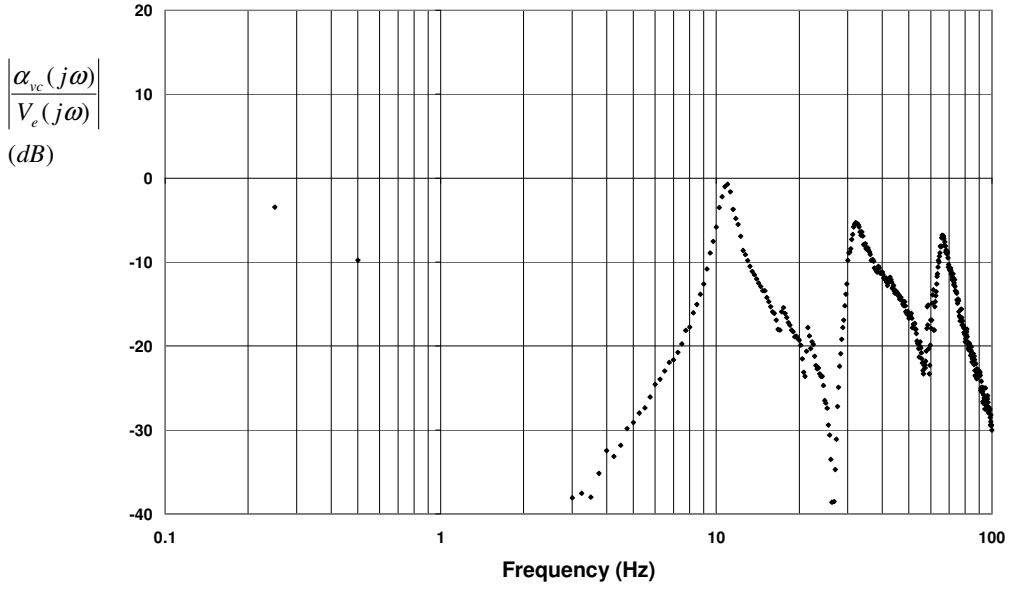


**Figure 5.10-** Closed-loop magnitude frequency response of the hydraulic simulator (input amplitude $0.1v$ or $2.3\ rad/s^2$).

### 5.4.3 Open-Loop Compensation

For the open-loop compensation study, a change in the approach of viewing data was made, that is testing shifted immediately to using the transient output waveform from the function generator as the input to the hydraulic simulator. This minimized the effects of drifting in the motor due to leakage and open-loop control. This became the procedure for the remaining tests and hence a frequency response was not done for the compensated open-loop system. Because the system was dismantled when this oversight was discovered, it was too late to do the open-loop compensated frequency response test. Thus the remaining results are presented in either a single frequency form or time response due to the transient form of the input signal.

In order to verify the model of the hydraulic simulator, a step input signal with the amplitude of $1v$ ( $23.0\ rad/s^2$ ) was applied to the system. The transient response of the hydraulic simulator is illustrated in Figure 5.11.

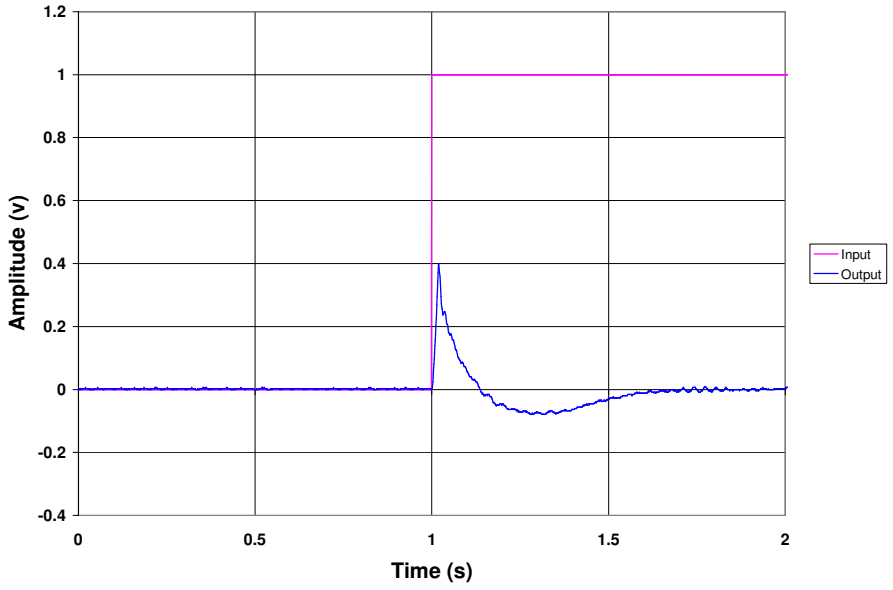


**Figure 5.11-** Open-loop transient response of the hydraulic simulator to a unit step input with amplitude of $1v$ ( $23.0\ rad/s^2$ )

Using the step response of the hydraulic simulator (shown in Figure 5.11) and the gain and lower cutoff frequency of the amplitude frequency response of the open-loop system (Figure 5.5), a first order transfer function was obtained and approximated to be $\frac{0.4s}{s+15.71}$. The response of this transfer function to the same input of Figure 5.11 is shown in Figure. 5.12. This model is consistent with the theoretical model proposed in Chapter 3 ($\frac{K_{OL}s}{\tau_o s+1}$). It should be noted that the experimental response does show an overshoot of the steady state value which the identified model does not. However, because the form of $\frac{0.4s}{s+15.71}$ was consistent with the theoretical model, it was decided to use this form to do initial designs of the compensator.

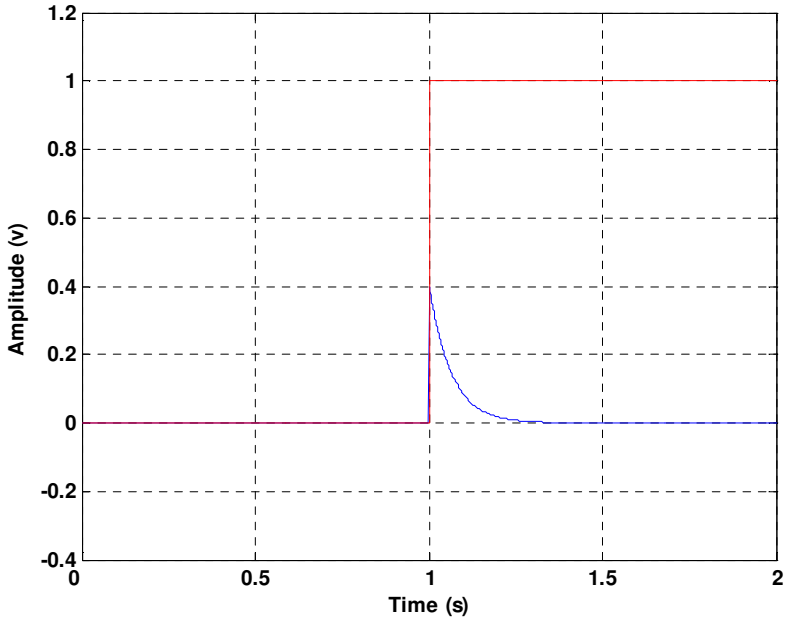


**Figure 5.12-** Transient response of the model ($\frac{0.4s}{s+15.71}$) to a unit step input signal (red line is the input and blue line is the output).

In this case, the open-loop compensator (inverse of the model of the hydraulic simulator) shown in Figure 3.15 was in the form of $\left(\frac{s+15.71}{0.4s}\right)$ or $\left(2.50+\frac{39.28}{s}\right)$. The test was performed by applying the compensator to the hydraulic simulator, but the system showed very erratic behavior. This indicated that the compensator gains were too high.

The compensator gains were then reduced and the tuned compensator which demonstrated reliable performance was in the form of $\left(\frac{s+15.71}{0.8s}\right)$ or $\left(1.25+\frac{19.64}{s}\right)$.

A set of tests was performed utilizing sine waves as the input signals with different amplitudes and frequencies and applying the open-loop compensator in the form of $\left(\frac{s+15.71}{0.8s}\right)$. Figures 5.13a and b illustrate the transient responses of the hydraulic simulator to the sine waves with frequency of 5 *Hz* and amplitudes of 1 and 2*v* respectively. The results showed acceptable responses for both two cases.

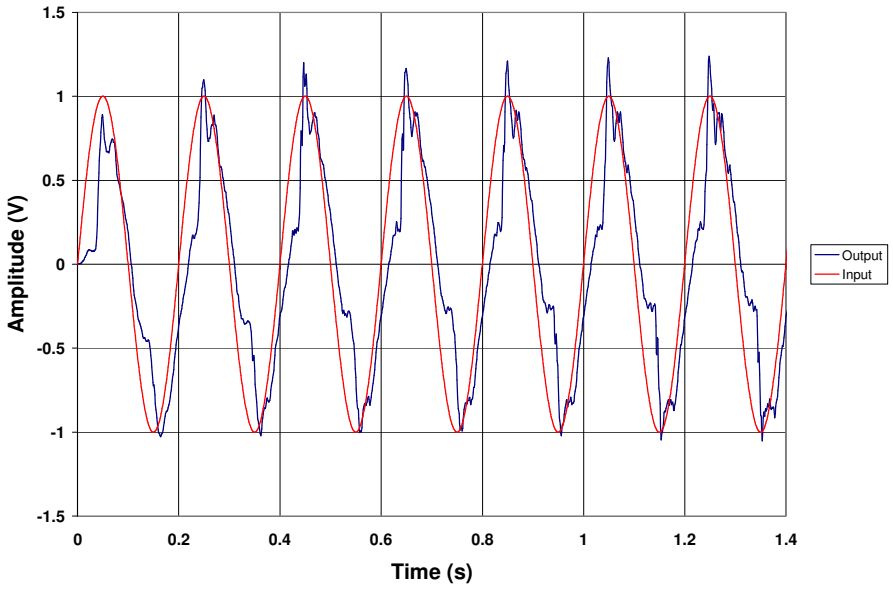


**Figure 5.13a-** Open-loop transient response of the hydraulic simulator to 5 *Hz* sine wave with amplitude of $1v$ (compensation $\frac{s+15.71}{0.8s}$)

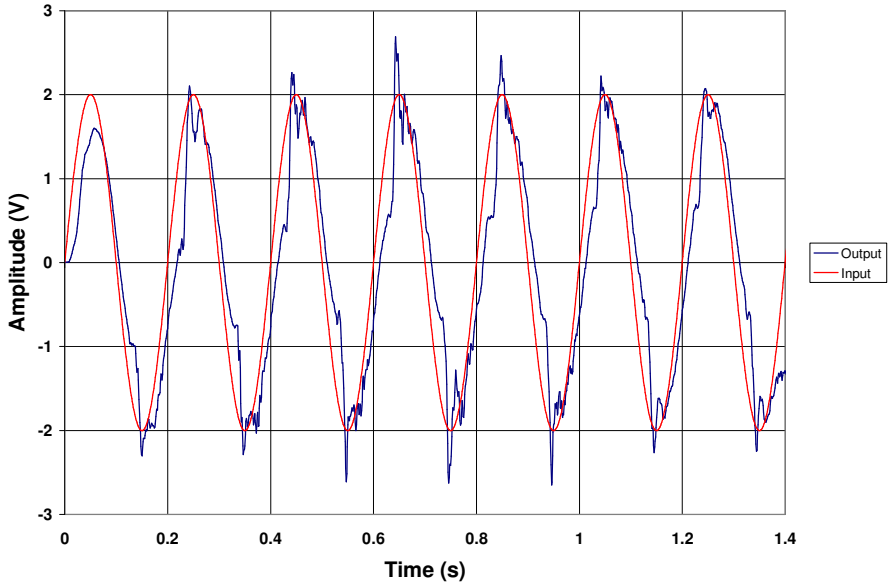


**Figure 5.13b-** Open-loop transient response of the hydraulic simulator to 5 *Hz* sine wave with amplitude of $2v$ (compensation $\frac{s+15.71}{0.8s}$)

Figures 5.14a and b demonstrate the transient responses of the hydraulic simulator to the sine wave input signals with frequency of 15 *Hz* and amplitudes of 1 and 2*v* respectively. The compensator in the form of $\frac{s+15.71}{0.8s}$ was used for both cases.

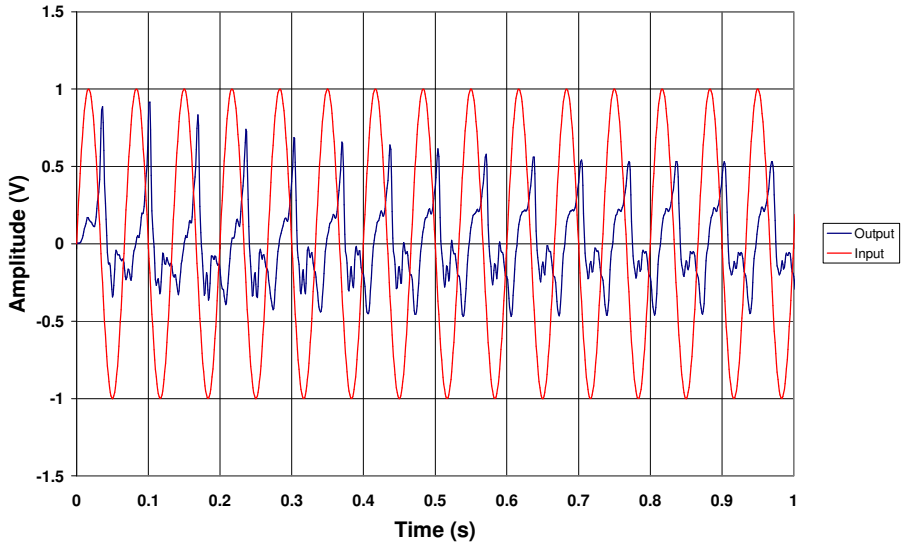


**Figure 5.14a-** Open-loop transient response of the hydraulic simulator to 15 *Hz* sine wave with amplitude of 1*v* (compensation $\frac{s+15.71}{0.8s}$)

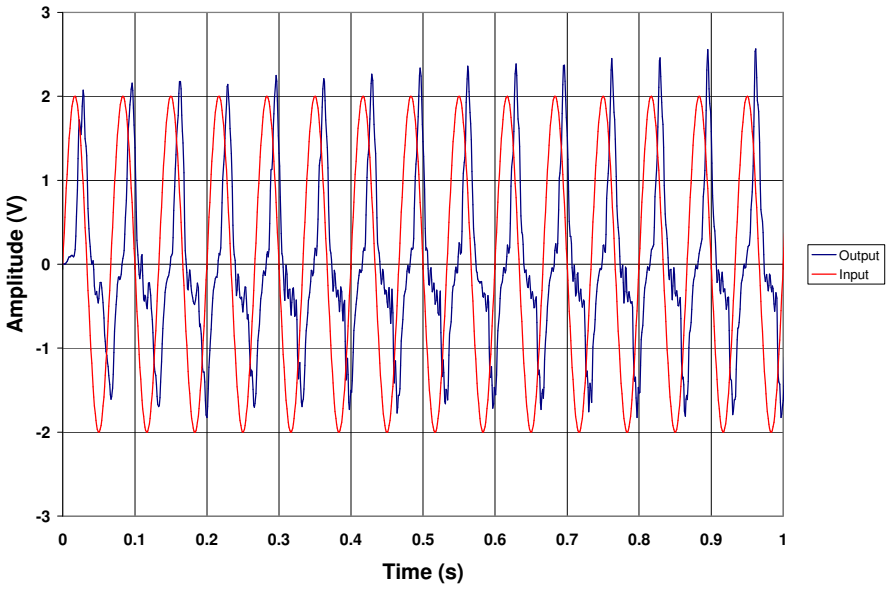


**Figure 5.14b-** Open-loop transient response of the hydraulic simulator to 15 *Hz* sine wave with amplitude of 2*v* (compensation $\frac{s+15.71}{0.8s}$)

It can be observed that the amplitude ratio for 1*v* input (Figure 5.14a) was not acceptable in comparison to the 2*v* input signal due to the significant nonlinearities in the rotary motor.

It may be concluded that the hydraulic simulator performance deteriorates at higher frequencies with the same input amplitude.

### 5.4.4 Transient Acceleration Responses

As mentioned in the previous section, the inverse compensator $\left(\frac{s+15.71}{0.4s}\right)$ could not be used due to the system erratic motion. Therefore a tuned compensator of the form $\left(\frac{s+15.71}{0.8s}\right)$ was applied to the system. In addition, two other compensators were tested

and compared with the lower gains. The compensators were in the form of $\left(\frac{s+8}{0.8s}\right)$ and $\left(\frac{s+4}{0.8s}\right)$.

In this section the transient responses of the hydraulic simulator to the function generator signals are shown. For each frequency, first the response of the system without applying any compensator is indicated. Then the responses of the system were illustrated by using the compensators $\left(\frac{s+4}{0.8s}\right), \left(\frac{s+8}{0.8s}\right)$ and $\left(\frac{s+15.71}{0.8s}\right)$ respectively.

#### 5.4.4.1 Frequency 5 *Hz* and Damping Ratio 0.1

Figures 5.15 to 5.18 show the experimental transient response of the hydraulic simulator to the desired acceleration for flexible joint manipulator for damping ratio of 0.1 and natural frequency of 5 *Hz*. Figure 5.15 does not contain any plant compensator. Figure 5.16 includes the compensator $\frac{s+4}{0.8s}$. Figure 5.17 includes the compensator $\frac{s+8}{0.8s}$. Finally, Figure 5.18 includes the compensator $\frac{s+15.71}{0.8s}$. In all cases, the manipulator follows the desired acceleration in an acceptable fashion but the addition of various compensators did not improve the responses at all. This is further demonstrated by calculating the tracking error and comparing the means squared error (MSE) of the tracking error. This comparison is tabulated in Table 5.1 at the end of the chapter.

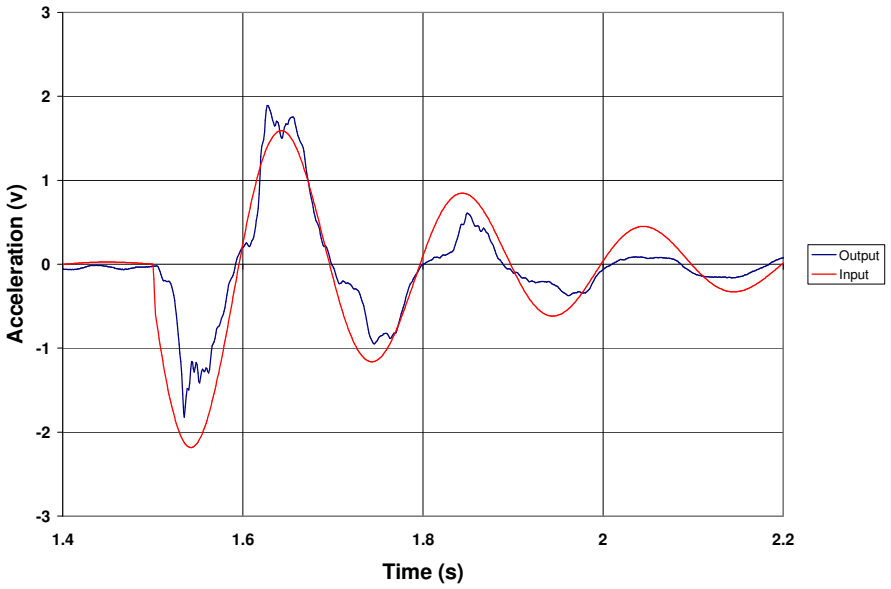


**Figure 5.15-** Open-loop transient response of the hydraulic simulator to the function generator 5 *Hz* and 0.1 damping ratio signal (not compensated).

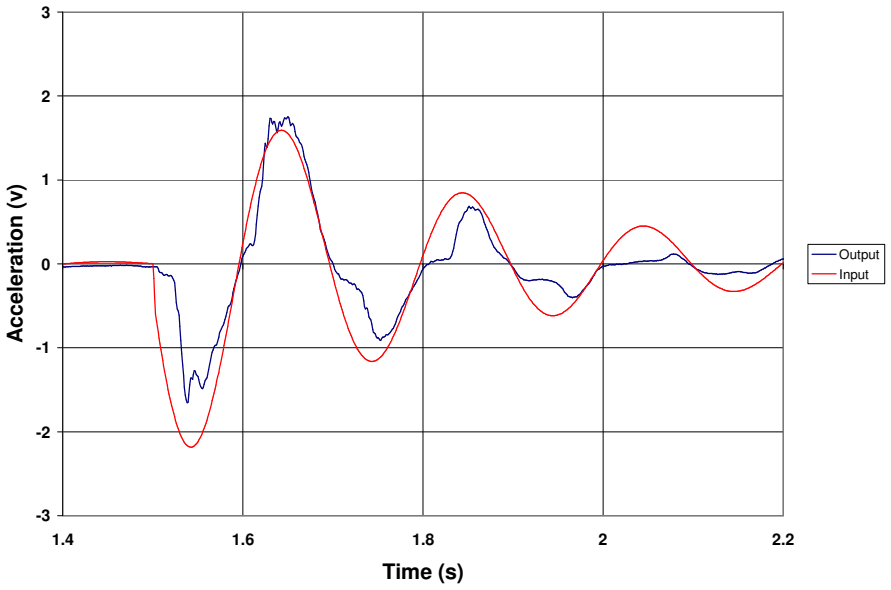


**Figure 5.16-** Open-loop transient response of the hydraulic simulator to the function generator 5 *Hz* and 0.1 damping ratio signal (compensated by $\frac{s+4}{0.8s}$)

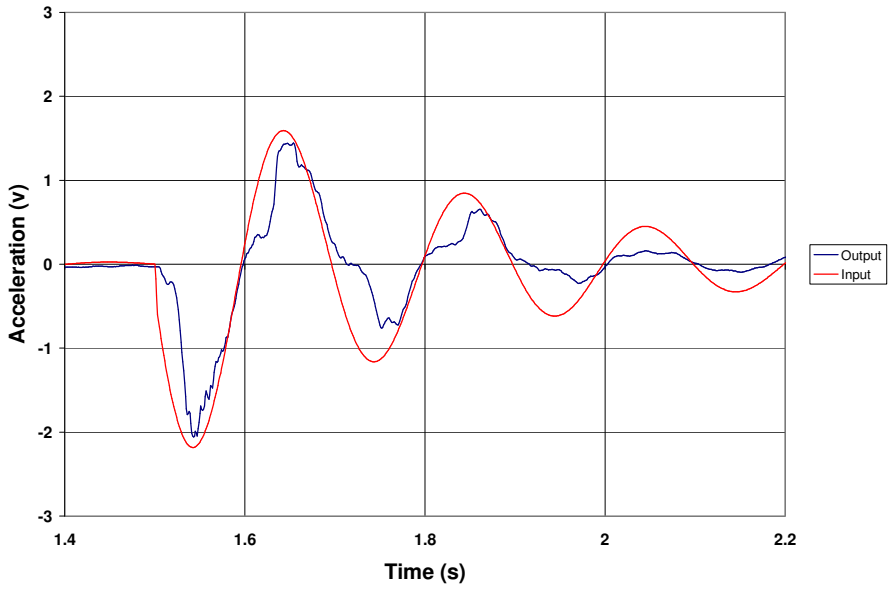


**Figure 5.17-** Open-loop transient response of the hydraulic simulator to the function generator 5 *Hz* and 0.1 damping ratio signal (compensated by $\frac{s+8}{0.8s}$).

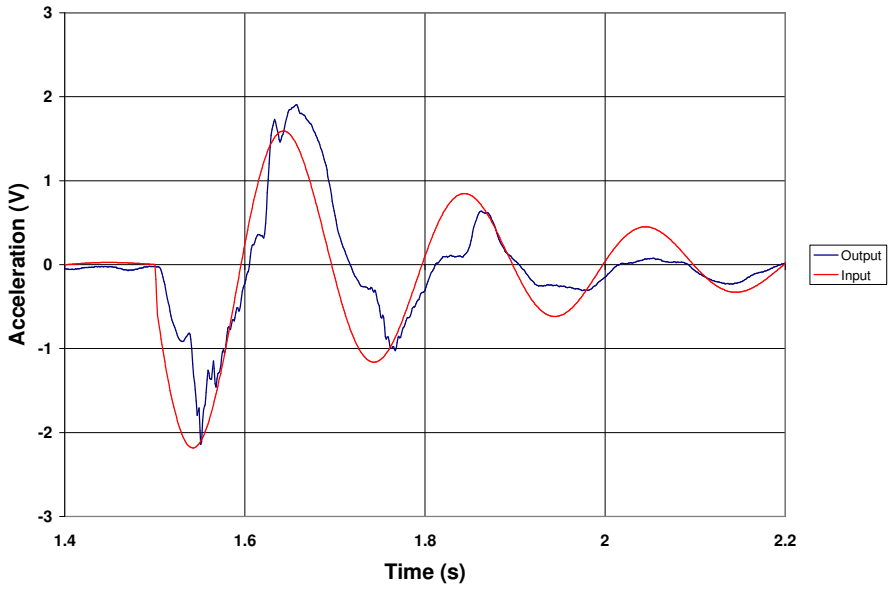


**Figure 5.18-** Open-loop transient response of the hydraulic simulator to the function generator 5 *Hz* and 0.1 damping ratio signal (compensated by $\frac{s+15.71}{0.8s}$)

### 5.4.4.2 Frequency 10 *Hz* and Damping Ratio 0.1

The same procedure used in 5.4.4.1 was repeated with an input frequency of 10 *Hz* and a damping ratio of 0.1. The transient responses are shown in Figure 5.19 for no compensation, Figure 5.20 for $\frac{s+4}{0.8s}$, Figure 5.21 for $\frac{s+8}{0.8s}$, and Figure 5.22 for $\frac{s+15.71}{0.8s}$. It is quite evident that the tracking capability of the hydraulic simulator deteriorates at this frequency. It was also noted that the addition of the compensators did not improve the responses which was consistent with that found in Section 5.4.4.1. The MSE was also determined for the tracking error and the results tabulated in Table 5.1

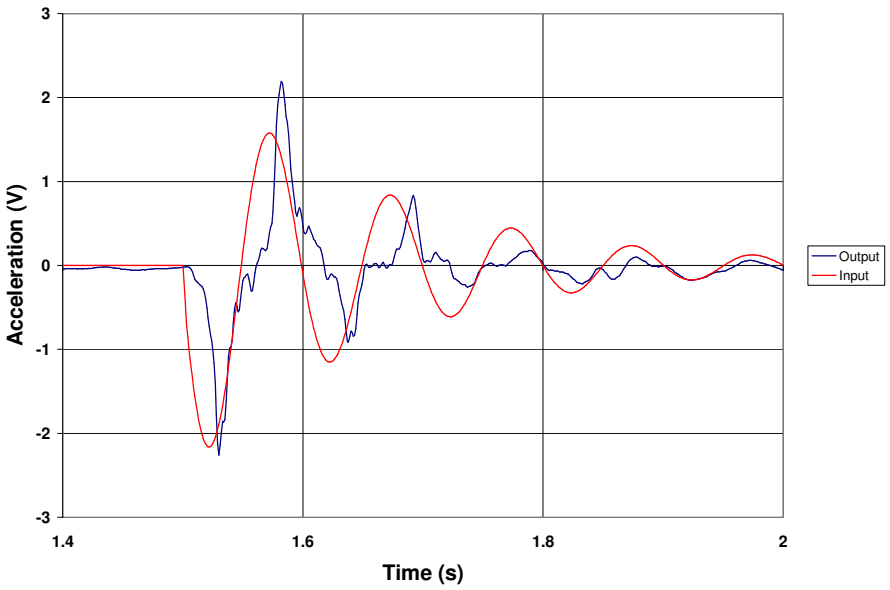


**Figure 5.19-** Open-loop transient response of the hydraulic simulator to the function generator 10 *Hz* and 0.1 damping ratio signal (not compensated).

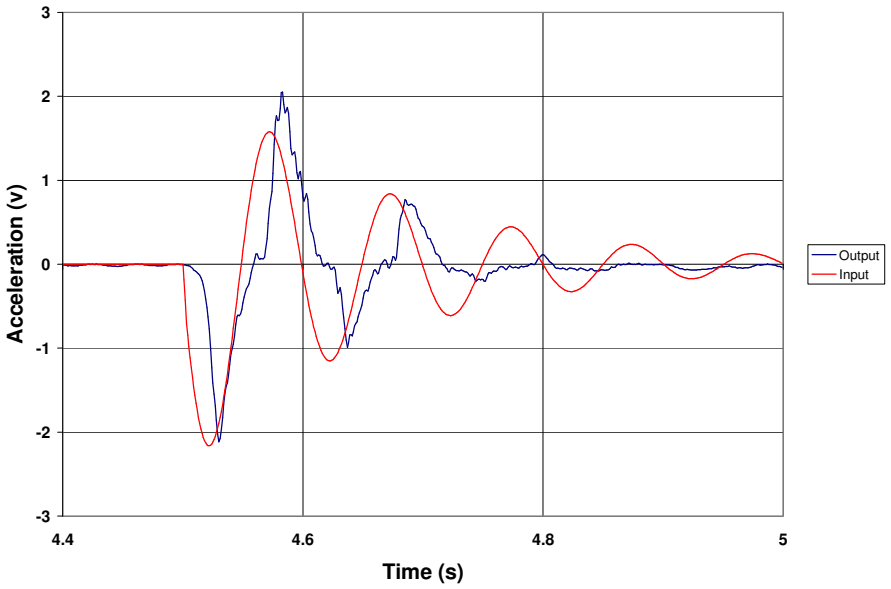


**Figure 5.20-** Open-loop transient response of the hydraulic simulator to the function generator 10 *Hz* and 0.1 damping ratio signal (compensated by $\frac{s+4}{0.8s}$).

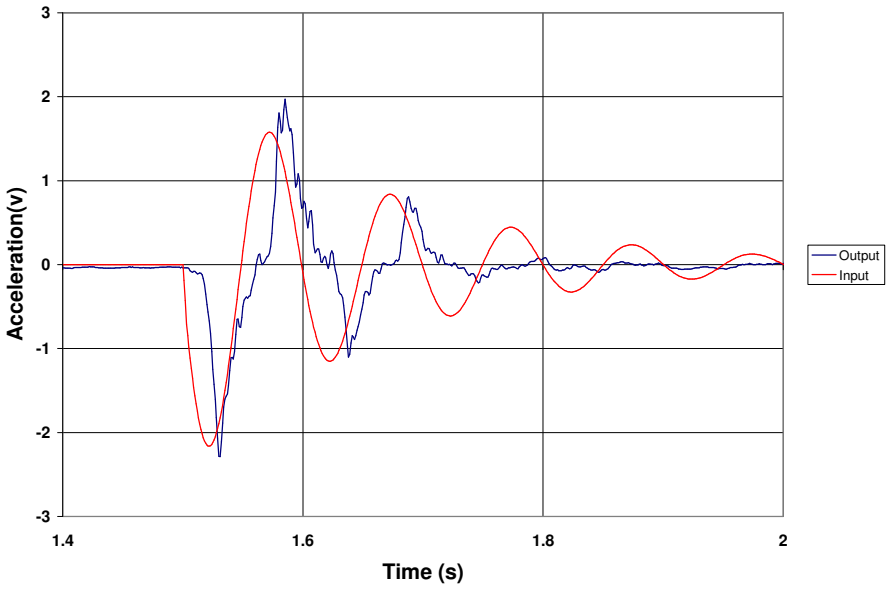


**Figure 5.21-** Open-loop transient response of the hydraulic simulator to the function generator 10 *Hz* and 0.1 damping signal (compensated by $\frac{s+8}{0.8s}$).

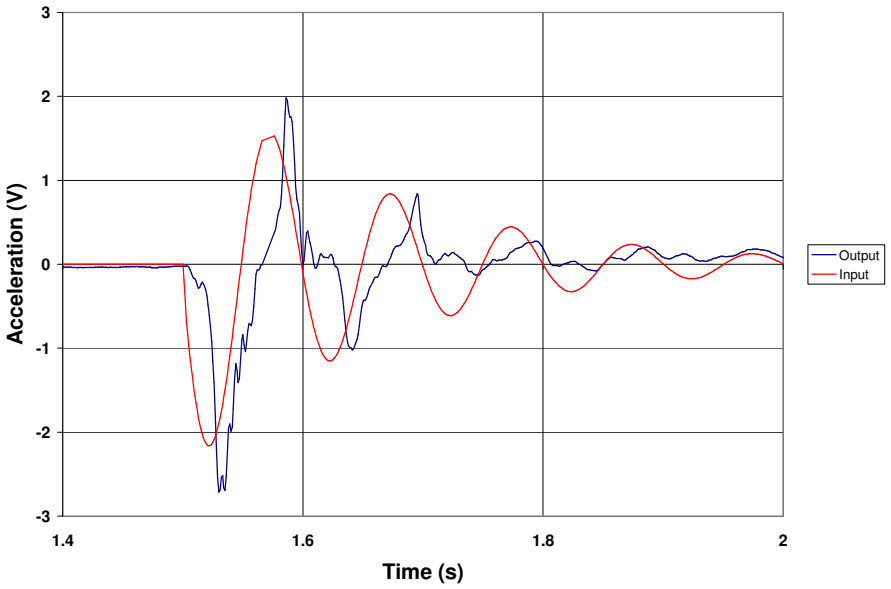


**Figure 5.22-** Open-loop transient response of the hydraulic simulator to the function generator 10 *Hz* and 0.1 damping ratio signal (compensated by $\frac{s+15.71}{0.8s}$)

### 5.4.4.3 Frequency 15 *Hz* and Damping Ratio 0.1

The same procedure used in 5.4.4.1 was repeated with an input frequency of 15 *Hz* and a damping ratio of 0.1. The transient responses are shown in Figure 5.23 for no compensation, Figure 5.24 for $\frac{s+4}{0.8s}$, Figure 5.25 for $\frac{s+8}{0.8s}$, and Figure 5.26 for $\frac{s+15.71}{0.8s}$. It is evident that the tracking capability of the hydraulic simulator deteriorates at this frequency but is similar to the results at 10 *Hz*. It was also noted that the addition of the compensators did not improve the responses which was consistent with that found in Sections 5.4.4.1 and 5.4.4.2. The MSE was also determined for the tracking error and the results tabulated in Table 5.1

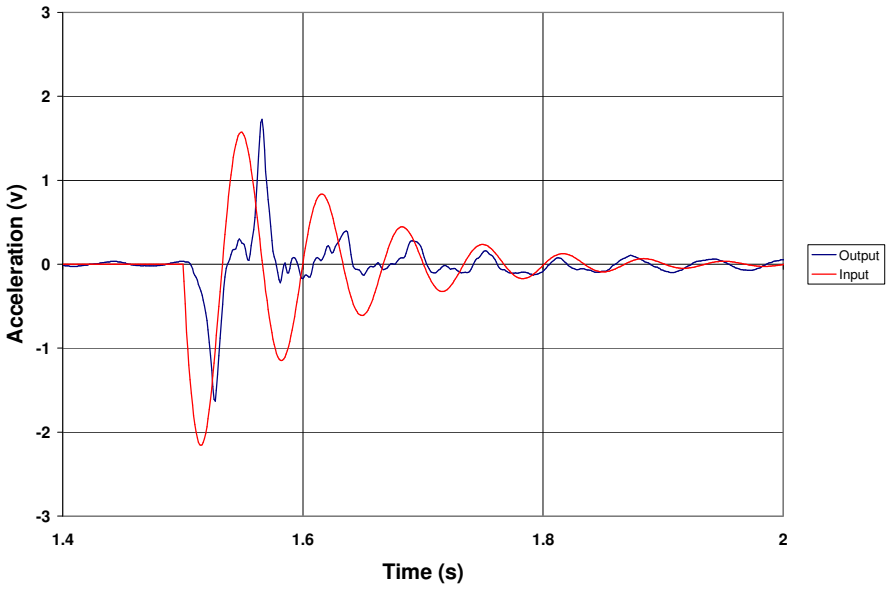


**Figure 5.23-** Open-loop transient response of the hydraulic simulator to the function generator 15 *Hz* and 0.1 damping ratio signal (not compensated).

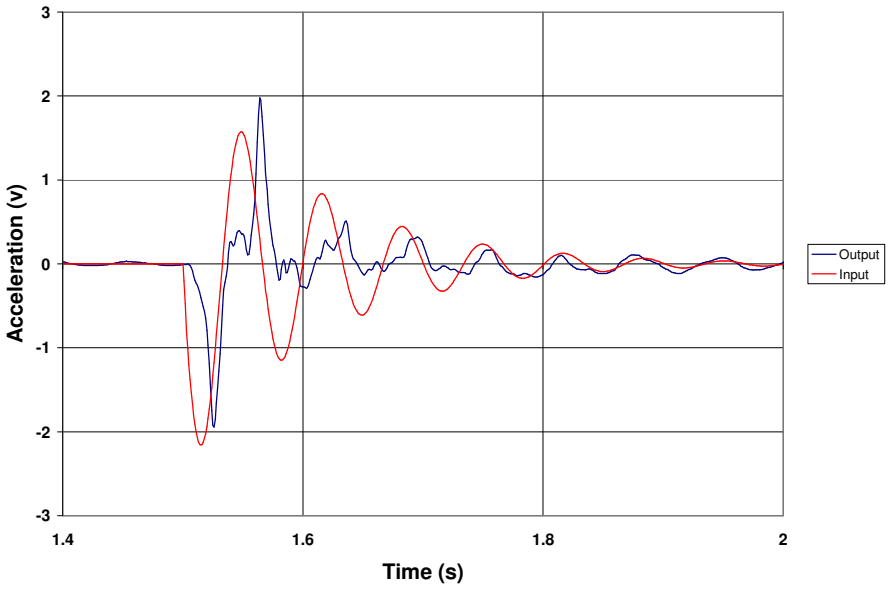


**Figure 5.24-** Open-loop transient response of the hydraulic simulator to the function generator 15 *Hz* and 0.1 damping signal (compensated by $\frac{s+4}{0.8s}$).

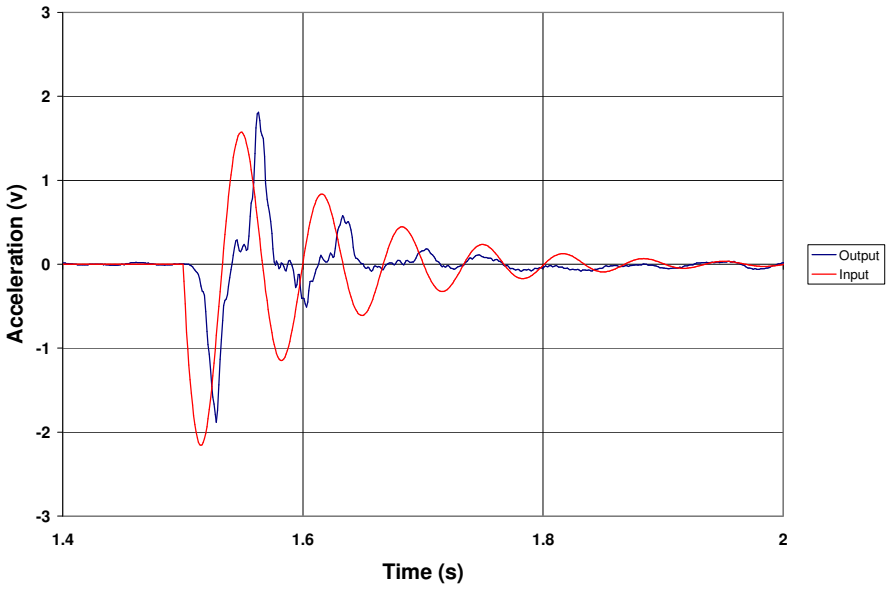


**Figure 5.25-** Open-loop transient response of the hydraulic simulator to the function generator 15 *Hz* and 0.1 damping signal (compensated by $\frac{s+8}{0.8s}$).

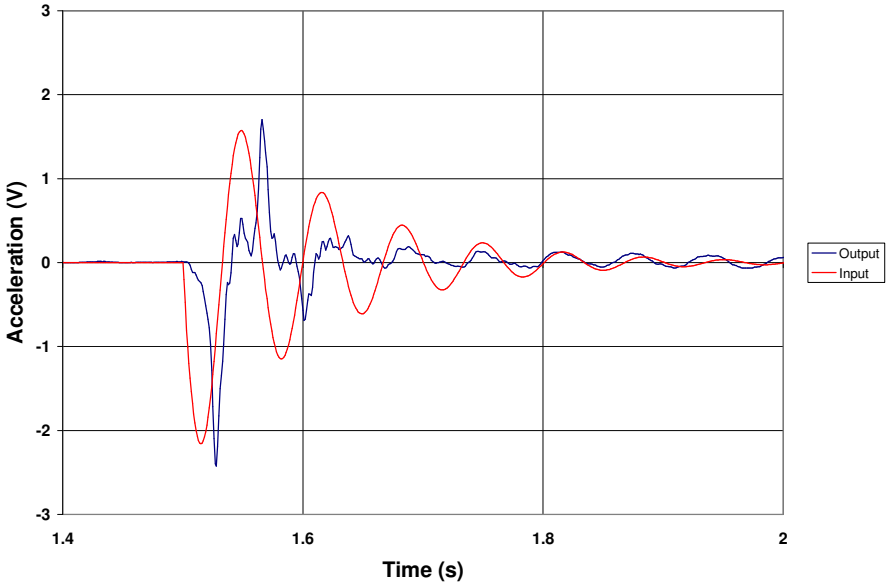


**Figure 5.26-** Open-loop transient response of the hydraulic simulator to the function generator 15 *Hz* and 0.1 damping ratio signal (compensated by $\frac{s+15.71}{0.8s}$).

### 5.4.5 Transient Response Errors

The acceleration tracking error is defined as the "actual acceleration – desired acceleration" or "output – input" of the hydraulic simulator transient response. The tracking error of the "not compensated" and "compensated by $\frac{s+15.71}{0.8s}$" plants for the transient responses presented in Sections 5.4.4.1, 5.4.4.2, and 5.4.4.3 are shown in Figures 5.27 to 5.32.

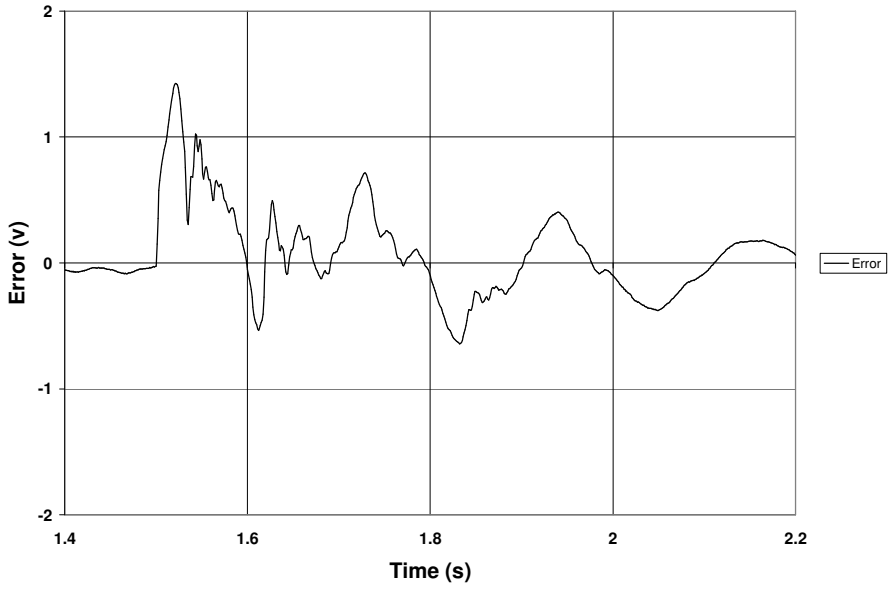


**Figure 5.27-** Tracking error of Figure 5.15 (frequency 5 *Hz* and damping ratio 0.1, not compensated)

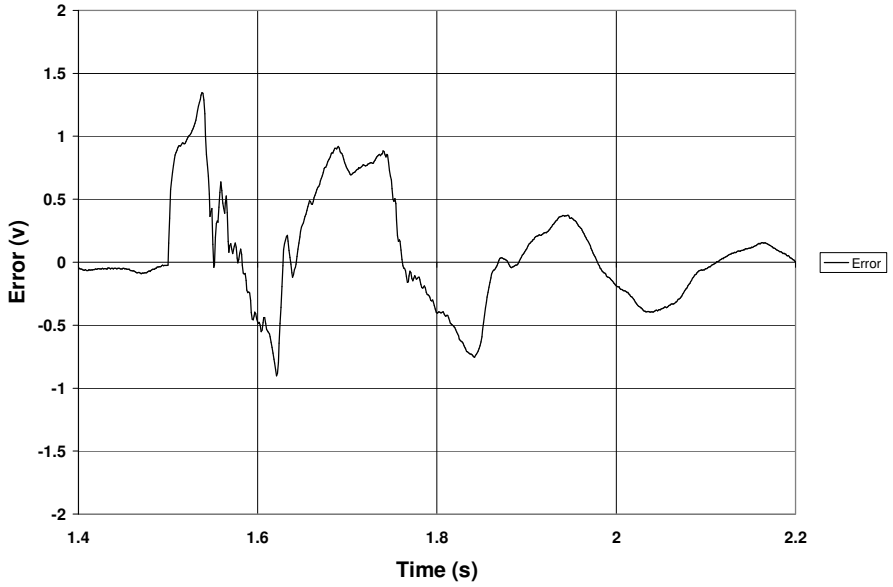


**Figure 5.28-** Tracking error of Figure 5.18 (frequency 5 *Hz* and damping ratio 0.1, compensated by $\frac{s+15.71}{0.8s}$)

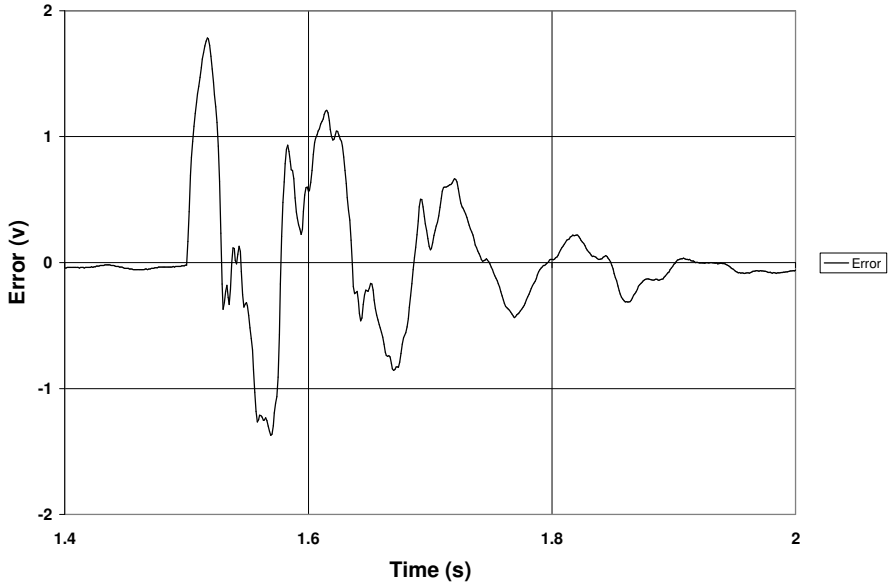


**Figure 5.29-** Tracking error of Figure 5.19 (frequency 10 *Hz* and damping ratio 0.1, not compensated)

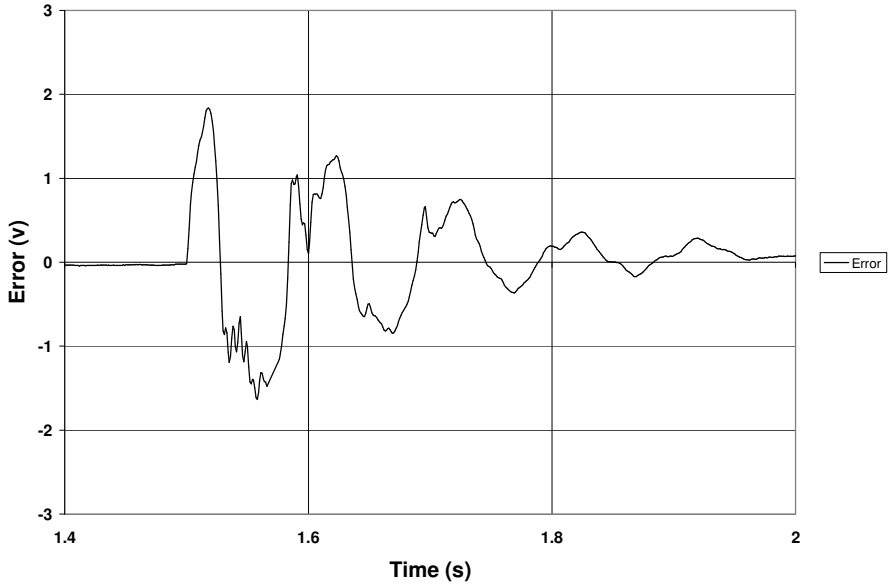


**Figure 5.30-** Tracking error of Figure 5.22 (frequency 10 *Hz* and damping ratio 0.1, compensated by $\frac{s+15.71}{0.8s}$)

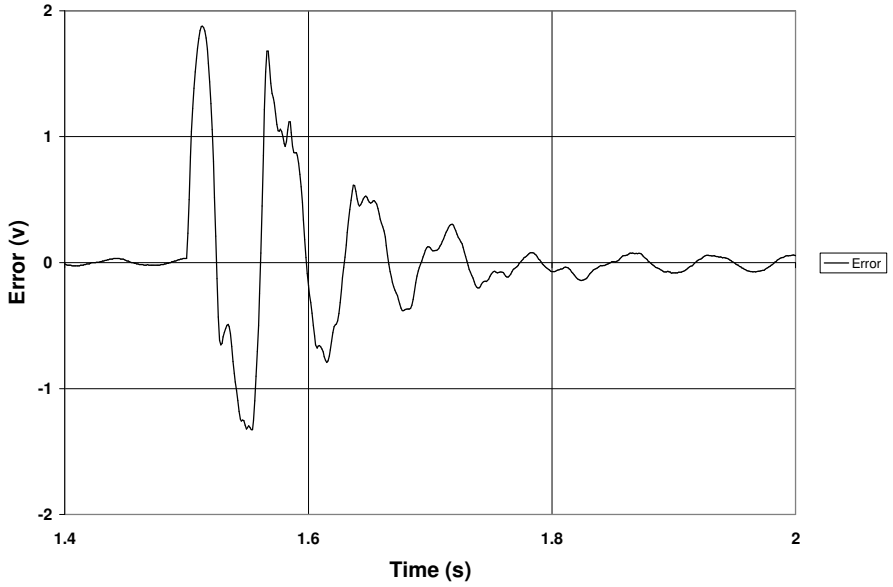


**Figure 5.31-** Tracking error of Figure 5.23 (frequency 15 *Hz* and damping ratio 0.1, not compensated)

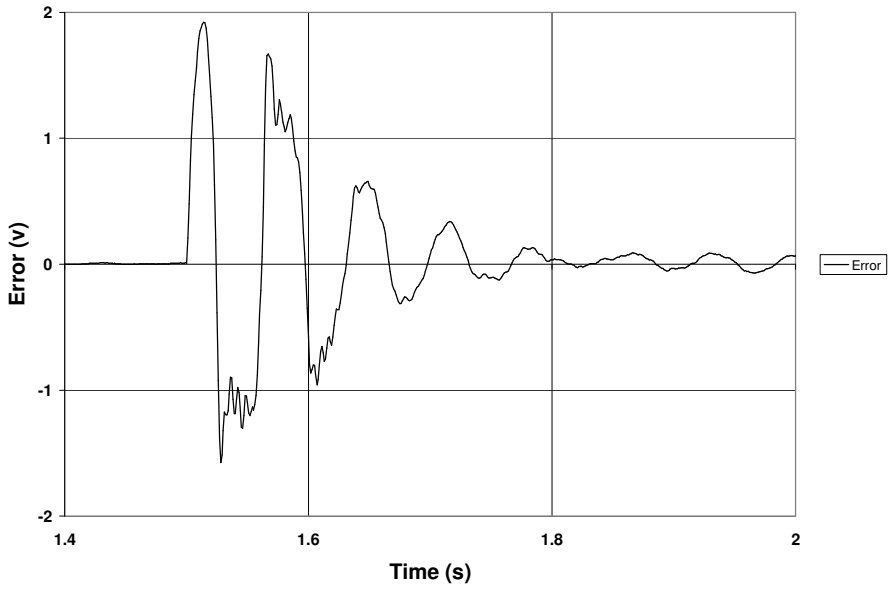


**Figure 5.32-** Tracking error of Figure 5.26 (frequency 15 *Hz* and damping ratio 0.1, compensated by $\frac{s+15.71}{0.8s}$)

The "Mean Squared Error" (MSE) values of the transient responses shown in Sections 5.4.4.1, 5.4.4.2, and 5.4.4.3 were calculated by using equation 5.1:

$$MSE = \frac{1}{n}\sum_{i=1}^{n} e_i^{\,2} \tag{5.1}$$

In this equation $e_i$ is the difference between the output and input of each data point and $n$ is the number of data. The MSE values are presented in Table 5.1:

**Table 5.1-** Mean squared error values of transient response errors in different cases

| Frequency ($Hz$) | Compensator | Duration Time (s) | MSE ($v^2$) |
|---|---|---|---|
| 5 | 1 | 1.4 to 2.0 | 0.162 |
| 5 | $\frac{s+4}{0.8s}$ | 1.4 to 2.0 | 0.169 |
| 5 | $\frac{s+8}{0.8s}$ | 1.4 to 2.0 | 0.193 |
| 5 | $\frac{s+15.71}{0.8s}$ | 1.4 to 2.0 | 0.240 |
| | | | |
| 10 | 1 | 1.4 to 2.0 | 0.253 |
| 10 | $\frac{s+4}{0.8s}$ | 1.4 to 2.0 | 0.310 |
| 10 | $\frac{s+8}{0.8s}$ | 1.4 to 2.0 | 0.304 |
| 10 | $\frac{s+15.71}{0.8s}$ | 1.4 to 2.0 | 0.321 |
| | | | |
| 15 | 1 | 1.4 to 2.0 | 0.238 |
| 15 | $\frac{s+4}{0.8s}$ | 1.4 to 2.0 | 0.236 |
| 15 | $\frac{s+8}{0.8s}$ | 1.4 to 2.0 | 0.268 |
| 15 | $\frac{s+15.71}{0.8s}$ | 1.4 to 2.0 | 0.276 |

It is interesting to note that the MSE at 10 *Hz* was greater than at 5 or 15 *Hz*. However, the MSE of the uncompensated system was consistently better than for any of the compensated plants. This perhaps reflects the concern flagged in the frequency response results in which the compensators "over compensated" the mid frequency range.

The transient and frequency responses clearly indicate the presence of very significant nonlinearities. Vandenberghe, who used the same system, identified the existence of severe dead-zone in the rotary motors [13]. The transient responses in this study give further evidence of dead-zone whose influence becomes more dominant as the amplitude of the input signal decreases.

# CHAPTER 6

# CONCLUSIONS AND RECOMMENDATIONS

## 6.1 Conclusions

As presented in section 1.3, the objective of this thesis was to design and implement an experimental hydraulic actuated robot manipulator that simulates robot joint flexibility in the specific range of frequencies and damping ratio with the ability of changing the joint flexibility's parameters. In other words, the main purpose of this research project was to analyze and control the "hydraulic simulator" in order to follow the signals produced by the "function generator" in a specific range of frequencies and damping ratio.

The attempt to apply closed-loop control was partially successful in the frequency response tests but when the transient response tests were conducted, the system behaved very erratically.

The approach for closed-loop control was based on classical PI techniques and clearly demonstrated that another more complex control strategy should be contemplated. Trying to control acceleration is a major challenge in the first place due to noise in the output signals. This when combined with the nonlinear behavior of the motor, severely limited the classical control approach. The study did, however, show that it was possible to compensate for poor transducer performance in the low frequency ranges, a problem which would have to be addressed regardless of the control approach used.

The open-loop transient response tests did not show the same erratic behavior as the closed-loop tests did. As a result only open-loop transient studies could be conducted. From the results presented in Chapter 5, it is evident that the addition of the compensators did little to improve the actual waveform of the experimental setup. Quite simply, nonlinearities "swamped" the behavior of the rotary motor. It was believed that the main contributing factor to these nonlinearities was due to dead-zone and quite possibly, the presence of stiction, hysteresis or material damping in the rotary motor.

The results shown in Chapter 5 are in fact acceptable given that the amplitude and frequency of the desired waveform can be reproduced by the hydraulic joint. There is a time delay in some of the peaks (further evidence of the dead-zone) and some distortion of the actual waveform but even these are considered acceptable for the prime users of the flexible joint simulator. Further, the range of frequencies (5 to 15 $Hz$) and damping ratio (0.1) was quite acceptable for flexible joint studies. Indeed, the ability to readily change these parameters is something that no known joint commercial simulator can readily do at present time.

In summary, although the ability of the proposed hydraulic joint to reproduce the desired waveforms was limited, it was concluded that the system was acceptable to conduct control studies for flexible joint robot manipulators.

## 6.2 Future Work

The objective of this research project was to initiate a study on the dynamic performance and to apply a control scheme to a robot manipulators with joint flexibilities by using a hydraulic actuated manipulator.

Since nonlinearities usually occur in hydraulic systems, the idea of utilizing more complex control strategies, especially nonlinear compensators rather than the classic strategies, could extend the acceptable performance range of the simulator. It is suggested that future studies involve more sophisticated controllers to overcome the effects that were experienced in this study if the existing components and transducers cannot be replaced.

It is further recommended that high precision rotary motors and measuring instruments such as accelerometers be used to replace those used in this study. This would expand the bandwidth of the hydraulic system, would reduce the noise associated with the measurements, and would increase the quality of the frequency response diagrams. Replacement would improve the capabilities of the hydraulic simulator; therefore a greater range of flexible joint robot manipulators could be studied.

Further to study of the joint flexibility in robot manipulators which was the purpose of this study, the hydraulic simulator can be used as a “general simulator” which is capable of following any input signals in a specific range of frequencies.

# REFERENCES

[1] De Luca, A.; and Tomei, P.; *Elastic Joints*. In Canudas de Wit, C.; Siciliano, B.; and Bastin, G.; editors, 1996, "*Theory of Robot Control*" Springer-Verlag, Berlin, Germany, pp.179-217, Chap. 5.

[2] Mario, R.; and Spong, M. W.; 1986, "*Nonlinear Control Techniques for Flexible Joint Manipulators: A Single Link Case Study*", Proceedings of IEEE International Conference on Robotics and Automation, Vol.2, pp.1030-1036.

[2] Nicosia, S.; Nicolo, F.; and Lentini, D., 1981, "*Dynamical Control of Industrial Robots with Elastic and Dissipative Joints*" Proceedings of 8th IFAC world congress, Kyoto, Japan, pp. 1933-1940.

[4] Spong, M.W.; 1987, "*Modeling and Control of Elastic Joint Robots*" Transactions ASME: Journal of Dynamic Systems, Measurements and Control, Vol.109, pp. 310-319.

[5] Yu, J. S.; Hu, R.; and Muller, P. C.; 1993, "*An Approach to Adaptive Decentralized Control of Flexible Joint Robots*", Proceedings of IEEE/RSJ International Conference on Intelligent Robots and Systems, pp.8-13.

[6] Albu-Schaffer, A.; and Hirzinger, G.; 2000, "*State Feedback Controller for Flexible Joint Robots: A Globally Stable Approach Implemented on DLR's Light-Weight Robots*" Proceedings of IEEE/RSJ Int. Conference on Intelligent Robots.

[7] Thummel, M.; Otter, M.; and Bals, J.; 2001, "*Control of Robots with Elastic Joints Based on Automatic Generation of Inverse Dynamics Models*" Proceedings of IEEE/RSJ Int. Conference on Intelligent Robots, pp. 925-930.

[8] Habibi, S. R.; Richards, R. J.; and Goldenberg, A. A.; 1994, "*Hydraulic Actuator Analysis for Industrial Robot Multivariable Control*" Proceedings of the American Control Conference, pp. 1003-1007

[9] Readman, M.C.; 1994, "*Flexible Joint Robots*" CRC Press, Boca Raton.

[10] Thayer, W. J.; 1965, "*Transfer Function for Moog Servovalves*" Technical Bulletin 103, MOOG® Inc.

[11] Moog Inc.; "*15 Series Servovalve: Performance Characteristics – Frequency Response*"

[12] Micromatic Inc.; "*Rotary Motor MPJ-22-1V*" catalogue

[13] Vandenberghe, G.; 1993, "*Conflicting Rule Based Learning Algorithm for Controlling A Hydraulic Robot*" Master Thesis, Department of Mechanical Engineering, University of Saskatchewan.

[14] Merritt, H. E.; 1967, "*Hydraulic Control Systems*" John Wiley & Sons, New York.